

Chapter 2

Vibrational Spectroscopy

2.1 Molecular Vibrations

A description of a quantum-mechanical system requires the knowledge of its Hamiltonian H . The solution of the time-independent Schrödinger equation gives the eigenstates and energies of a molecule whereas the time evolution, e.g., arising from interactions with a fluctuating solvent or a light field, is determined by the time-dependent Schrödinger equation. Consider as a starting point the following Hamiltonian of a molecule:

$$H = -\frac{\hbar^2}{2m_e} \sum_i \nabla_e^2 - \sum_i \frac{\hbar^2}{2m_{n,i}} \nabla_n^2 + V_{ee} + V_{nn} + V_{ne} \quad (2.1)$$

The first two terms on the right-hand side represent the kinetic energies with the sum running over all electrons and nuclei with the masses m_e and $m_{n,i}$, respectively. The Laplace operators $\nabla_{e,n}^2$ act either on the electronic (e) or nuclear (n) coordinates. V_{ee} and V_{nn} are due to the electrons' and nuclei's Coulomb repulsion whereas the term V_{ne} describes the Coulomb attraction between electrons and nuclei. We only include terms for an isolated molecule. In the liquid phase, additional terms due to solute-solvent interactions contribute to the Hamiltonian.

In the Born-Oppenheimer approximation [1], a separation between the electronic and nuclear wavefunctions due to their distinctly different masses and time scales of motion leads to a situation where the electronic states define potential energy surfaces for the nuclei. Figure 2.1 schematically shows the vibrational potential $V(q)$ as a function of the vibrational coordinate q , e.g., the distance of two atoms in a molecule. Around the equilibrium distance q_0 , the potential might be approximated as harmonic. However, large nuclear separations will eventually lead to bond dissociation and at short separations the repulsion terms in Eq. 2.1 dominate, effectively causing the potential to be anharmonic. Intra- and intermolecular vibrational couplings are additional sources for anharmonicities of polyatomic molecules in the condensed phase. As a consequence, the energy levels are not equally spaced and the diagonal anharmonicity $\Delta = E_{01} - E_{12}$ is a sensitive probe for the local structure and interactions of a molecule. Here, $E_{01} = E_1 - E_0$ and $E_{12} = E_2 - E_1$ represent

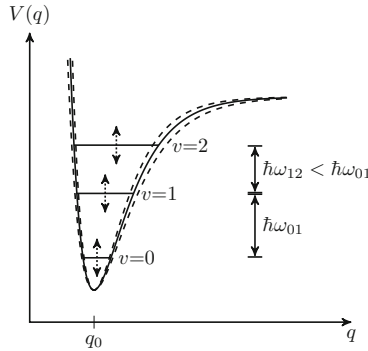


Fig. 2.1 Anharmonic oscillator potential. The anharmonicity causes the transition frequency ω_{01} for the $v = 0$ to 1 transition to be bigger than the one for the $v = 1$ to 2 transition (ω_{12}). Fluctuating forces exerted by the bath cause a time-dependent potential (*dashed lines*) resulting in fluctuating transition frequencies

the energy differences for transitions from the ground to the first excited state ($v = 0$ to 1) and from the first to the second excited state ($v = 1$ to 2), respectively. Instead of energies, this thesis we will often use transition frequencies $\omega_{01,12} = E_{01,12}/\hbar$ that are commonly measured in wavenumbers $\nu = \omega/(2\pi c)$ (with c being the speed of light) in infrared spectroscopy.

Infrared spectra are closely related to the vibrational potential $V(q)$. Numerous textbooks cover a large variety of aspects related to the structure and interaction of complex molecules and their connection to vibrational absorption spectra. A few of them will be reviewed in the next section that is mainly based on [2–4].

2.1.1 Vibrational Structure of Polyatomic Molecules

A molecule consisting of N atoms has $3N$ degrees of freedom, 6 of which describe the translation of the center of mass and the molecular rotation; i.e., there are $3N - 6$ vibrational degrees of freedom described by the coordinates $\vec{q} = (q_1, \dots, q_m)$ with $m = 3N - 6$. If the nuclear displacements from their equilibrium positions are small, the vibrational potential $V(\vec{q})$ can be approximated with a Taylor expansion:

$$V(\vec{q}) = V(\vec{q}_0) + \sum_{i=1}^m \left. \frac{\partial V}{\partial q_i} \right|_{\vec{q}_0} q_i + \frac{1}{2} \sum_{i,j=1}^m \left. \frac{\partial^2 V}{\partial q_i \partial q_j} \right|_{\vec{q}_0} q_i q_j + \frac{1}{6} \sum_{i,j,k=1}^m \left. \frac{\partial^3 V}{\partial q_i \partial q_j \partial q_k} \right|_{\vec{q}_0} q_i q_j q_k + \dots \quad (2.2)$$

$$\approx \frac{1}{2} \sum_{i,j=1}^m V_{ij}(\vec{q}_0) q_i q_j + \dots \quad (2.3)$$

$V(\vec{q}_0)$ is the (constant) potential at the equilibrium position that can be defined as zero. $\partial V/\partial q_i|_{\vec{q}_0}$ is the force acting on the i th coordinate that vanishes at the equilibrium position so that the quadratic term is the leading one in the Taylor expansion. By neglecting higher-order terms in Eq. 2.3, the harmonic approximation is applied. A diagonalization of the quadratic Hamiltonian is achieved by a coordinate transformation to normal modes [5]. As a result, the well-known energy structure of quantum-mechanical harmonic oscillators [6] is obtained

$$E(v_1, \dots, v_m) = \sum_{i=1}^m \hbar \omega_i \left(v_i + \frac{1}{2} \right) \quad (2.4)$$

with the frequency ω_i and vibrational quantum number v_i of the i th normal mode. The corresponding wavefunction is a product of wavefunctions of m independent oscillators.

As pointed out before, realistic vibrational potentials of molecules in solution are anharmonic, i.e., higher-order terms in Eq. 2.3 cannot be neglected. Consequently, the vibrational energies are not simple sums of individual oscillators but may be approximated

$$E(v_1, \dots, v_m) \approx \sum_{i=1}^m \hbar \omega_i \left(v_i + \frac{1}{2} \right) + \sum_{i=1}^m \sum_{k \geq i}^m x_{ik} \left(v_i + \frac{1}{2} \right) \left(v_k + \frac{1}{2} \right) + \dots \quad (2.5)$$

where the factors x_{ik} represent the anharmonicity constants. Similarly, the total vibrational wavefunction depends on the anharmonicities and is no longer a product of single harmonic oscillator wavefunctions.

Note that the vibrational energy levels are not equidistant when anharmonicities are included. If the off-diagonal anharmonicities x_{ik} with $i \neq k$ vanish, we find for the transition energy difference of the i th mode $\Delta_i = E_{01i} - E_{12i} = -2x_{ii}$. The diagonal anharmonicities x_{ii} are typically negative leading to a red-shifted excited state absorption (cf. Fig. 2.7). Likewise, non-vanishing off-diagonal anharmonicities lead to changes of the transition frequency of oscillator i according to the value of x_{ik} and the population of oscillator k . While diagonal anharmonicities of vibrations are of major importance in time-resolved vibrational spectroscopy when an excited state population exists, the subsequent relaxation and population of low-frequency bath modes often cause long-lived heating signals due to the off-diagonal anharmonicities.

An important consequence following from the introduction of mixed terms $q_i q_j$ with $i \neq j$ in Eq. 2.3 is that originally degenerate levels will split in energy. Consider two eigenstates $|\varphi_{1,2}\rangle$ with energies $E_1^0 \approx E_2^0$ of the uncoupled Hamiltonian H_0 that is purely quadratic in the coordinate q_i . The degeneracy is lifted by searching for new eigenstates $|\tilde{\varphi}_{\pm}\rangle$ of the Hamiltonian $H = H_0 + H'$ including coupling terms H' . The corresponding new energies E_{\pm} follow from the secular determinant:

$$\begin{vmatrix} E_1^0 - E_{\pm} & H'_{12} \\ H'_{21} & E_2^0 - E_{\pm} \end{vmatrix} = 0 \quad (2.6)$$

Here H'_{12} and $H'_{21} = H_{12}^{*\prime}$ are the matrix elements of the coupling Hamiltonian between the old $|\varphi_{1,2}\rangle$ -states. The solution to Eq. 2.6 is

$$E_{\pm} = \bar{E}^0 \pm \frac{1}{2} \sqrt{4 |H'_{12}|^2 + \delta^2} \quad (2.7)$$

with $\bar{E}^0 = (E_1^0 + E_2^0)/2$ and $\delta = E_2^0 - E_1^0$ being the average and difference of E_1^0 and E_2^0 , respectively. In the weak-coupling limit ($|H'_{12}| \ll \delta$), the eigenstates and energies are only slightly altered so that energy difference $E_+ - E_- \approx \delta$. Obviously, splitting of (nearly) degenerate levels occurs in the strong-coupling limit ($|H'_{12}| \gg \delta$). Hence, the degeneracy is removed ($E_+ - E_- \approx 2|H'_{12}|$) and the new eigenstates are superpositions of $|\varphi_{1,2}\rangle$ whose degree of mixing increases with the coupling matrix element $|H'_{12}|^2$.

Consider, e.g., the two local OH stretching modes of a water molecule resulting from independent oscillations of the two hydrogens. For two oscillators without coupling these vibrations would be degenerate. That is, the two eigenstates $|\varphi_1\rangle = |10\rangle$ and $|\varphi_2\rangle = |01\rangle$ have the same eigenfrequency. Using the annihilation and creation operators $a_{1,2}$ and $a_{1,2}^\dagger$ acting only on the corresponding wavefunction it follows that $q_1 q_2 \propto (a_1 + a_1^\dagger)(a_2 + a_2^\dagger)$. Only the term $a_1^\dagger a_2$ survives in calculating $H'_{12} = \langle \varphi_1 | q_1 q_2 | \varphi_2 \rangle$ demonstrating that the mixed terms in Eq. 2.3 indeed lead to a splitting of energy levels. For the water molecule the new eigenstates are the normal symmetric and antisymmetric stretching modes with the wavefunctions $|\varphi_{S,AS}\rangle = 1/\sqrt{2} (|01\rangle \pm |10\rangle)$ (cf. Sect. 2.1.4).

Degeneracies also occur when a combination or overtone of a vibration has a similar frequency as another high-frequency vibration. This phenomenon of a so-called accidental degeneracy was first observed by Fermi for vibrations of CO_2 molecules [7]. It is therefore often referred to as *Fermi resonance*. In bulk water, the OH bending overtone ($v = 2$) is close in energy to the broad stretching band. The corresponding coupling matrix element is $\langle 20 | H' | 01 \rangle$. Apparently, at least third-order terms of the potential have to be considered, e.g., $q_1^2 q_2$ produces (amongst others) the combination $a_1^{\dagger 2} a_2$ that results in a non-vanishing matrix element. Generally, Fermi resonances and the accompanying level mixing lead to enhancements of the oscillator strength of overtones which also serve as energy acceptors for vibrational excitations of the high-frequency mode. It will be shown in this work that the bending mode plays an important role for OH stretching excitations of phospholipid hydration shells.

There are different methods to access vibrational frequencies of molecules in the electronic ground state, e.g., infrared absorption, Raman scattering [8] and inelastic neutron scattering [9]. In this thesis we will focus on the first technique which is based on the interaction of molecular dipoles with an infrared electric light field. According to Fermi's Golden rule, the probability of a transition from an initial state $|\varphi_i\rangle$ to a final state $|\varphi_f\rangle$ caused by the dipole interaction is determined by the dipole

matrix element $|\mu_{if}|^2 = |\langle \varphi_i | \mu | \varphi_f \rangle|^2$. A Taylor expansion of the dipole moment μ with respect to the coordinate of a molecular vibration q around the equilibrium position q_0

$$\mu(q) = \mu(q_0) + \left. \frac{\partial \mu}{\partial q} \right|_{q_0} q + \dots \quad (2.8)$$

shows that transitions between orthogonal states only occur if there is a change of the dipole $\partial \mu / \partial q|_{q_0}$ since $\mu(q_0)$ is a constant that represents the equilibrium dipole moment.

Dipole-allowed transitions give rise to infrared absorption lines [10]

$$A(\omega) \propto \int_{-\infty}^{\infty} e^{-i\omega t} \langle \mu(t) \mu(0) \rangle dt \quad (2.9)$$

at characteristic vibrational frequencies ω . That is, the infrared absorption is determined by the Fourier transform of the ensemble-averaged dipole time correlation function (the ensemble average is denoted by $\langle \rangle$). Ensemble-averaging is necessary in condensed-phase systems due to the variety of molecular conformations arising from the interaction with their environment. A statistical description of such systems is obtained with a density matrix formulation. Using the density matrix ρ , the ensemble average of an observable A follows from the evaluation of the trace:

$$\langle A \rangle = \text{Tr}[A\rho] \quad (2.10)$$

In liquid-phase vibrational spectroscopy, the surrounding solvent can often be treated as a heat bath. At finite temperature, thermal fluctuations of the bath cause fluctuating forces on vibrational coordinates. Therefore, such fluctuations directly contribute to the infrared lineshapes through the time correlation function in Eq. 2.9. The theoretical framework of lineshape analysis was initially formulated for the interpretation of NMR spectra [11–13] and later adopted for vibrational spectroscopy [14]. In the following, the main concepts that are necessary to extract time-resolved information from infrared spectra are briefly summarized.

2.1.2 Vibrational Lineshapes

It is assumed that the interaction between a molecule's vibrational mode and the bath is weak and that the bath is in thermal equilibrium (Markovian approximation). The Hamiltonian reads:

$$H = H_0 + H_B + H_{int} \quad (2.11)$$

Here, H_0 , H_B and H_{int} describe the vibrational degrees of freedom under consideration, the bath modes and the interaction between the vibrations and the bath, respectively. The eigenstates of H_B are inter- and intramolecular modes of the solvent or low-frequency modes of the solute itself. Typical interactions between the system and the bath arise from hydrogen bonding or other dipole-dipole interactions as well as long-range Coulomb forces. Due to the fluctuating forces originating from thermal fluctuations of the bath, the vibrational potential energy surface will change in time leading to a time-dependent transition frequency $\omega_{01}(t) \equiv \omega(t)$ (cf. Fig. 2.1) with:

$$\omega(t) = \omega_0 + \delta\omega(t) \quad (2.12)$$

Here $\delta\omega(t)$ is the time-dependent deviation from the time-averaged frequency ω_0 . The time scale of fluctuations directly reflects structural dynamics which are ultimately to be measured by time-resolved vibrational spectroscopy. Based on Eq. 2.12, one calculates the variance of frequency fluctuations $\Delta\omega$ and the correlation time τ_C :

$$\Delta\omega = \sqrt{\langle \delta\omega^2 \rangle} \quad (2.13)$$

$$\tau_C = \frac{1}{(\Delta\omega^2)} \int_0^\infty \langle \delta\omega(t) \delta\omega(0) \rangle dt \quad (2.14)$$

Using these definitions, one defines the fast-modulation limit ($\Delta\omega\tau_C \ll 1$) in which the correlation between transition frequencies is quickly lost whereas the transition frequencies maintain their correlation in the slow-modulation limit ($\Delta\omega\tau_C \gg 1$). In essence, τ_C quantifies the decay of the *frequency fluctuation correlation function* (FFCF):

$$C(t) = \langle \delta\omega(t) \delta\omega(0) \rangle \quad (2.15)$$

The FFCF correlates frequency fluctuations at two different instants in time, thereby measuring how long the memory of a molecule's vibrational frequency is preserved. Frequency distributions due to heterogeneous molecular conformations are taken into account by applying the ensemble average so that the FFCF is a fundamental quantity to characterize time-dependent transition frequencies in condensed-phase systems.

The random modulation of a transition frequency $\omega(t)$ may be expressed by the equation of motion for the corresponding dipole moment

$$\dot{\mu}(t) = -i\omega(t)\mu(t) \quad (2.16)$$

with the formal solution:

$$\begin{aligned}\mu(t) &= \mu(0) \exp \left(-i \int_0^t \omega(t') dt' \right) \\ &= \mu(0) e^{-i\omega_0 t} \underbrace{\exp \left(-i \int_0^t \delta\omega(t') dt' \right)}_{\phi(t)}\end{aligned}\quad (2.17)$$

Substitution of Eq. 2.17 into 2.9 shows that the absorption profile centered at ω_0 is determined by the time-dependence of the relaxation function $\phi(t)$. The ensemble average $\langle \phi(t) \rangle$ describes the loss of coherence of initially coherent oscillators due to their fluctuating transition frequencies. Using a cumulant expansion one can show that [12]

$$\langle \phi(t) \rangle \approx \exp(-g(t)) \quad (2.18)$$

$$g(t) = \frac{1}{2} \int_0^t \int_0^t dt' dt'' \langle \delta\omega(t') \delta\omega(t'') \rangle \quad (2.19)$$

Equation 2.18 is exact for Gaussian frequency fluctuations. The equations above connect microscopic information in the form of the FFCF to experimentally observable infrared lineshapes. For stationary processes $\langle \delta\omega(t') \delta\omega(t'') \rangle$ is a function of the time difference $\tau = t'' - t'$ and the lineshape function $g(t)$ becomes:

$$g(t) = \int_0^t d\tau (t - \tau) \langle \delta\omega(\tau) \delta\omega(0) \rangle \quad (2.20)$$

In the Markovian limit, the FFCF may be approximated by an exponential decay so that:

$$\begin{aligned}g(t) &= (\Delta\omega)^2 \int_0^t d\tau (t - \tau) e^{-t/\tau_C} \\ &= (\Delta\omega)^2 \tau_C^2 (e^{-t/\tau_C} + t/\tau_C - 1)\end{aligned}\quad (2.21)$$

For slow frequency modulations, the exponential can be expanded in a Taylor series so that the leading term of the lineshape function is $g(t) \approx 1/2 (\Delta\omega)^2 t^2$. Consequently, a Gaussian infrared absorption profile of $\Delta\omega$ width will be observed directly reflecting the frequency spread of a static distribution of oscillators. The corresponding line broadening is therefore called *inhomogeneous* broadening. Fast frequency modulations lead to a linear lineshape function of $g(t) = (\Delta\omega)^2 \tau_C t$. As a result, the infrared absorption profile is a Lorentzian displaying a *homogeneous* linewidth $\Delta\omega_{hom}$ that is the inverse of the pure dephasing time T_2^* :

$$\Delta\omega_{hom} = \frac{2}{T_2^*} \quad (2.22)$$

$$T_2^* = \frac{1}{(\Delta\omega)^2 \tau_C} \quad (2.23)$$

Obviously, the linewidth decreases with decreasing correlation times τ_C . Due to the fast frequency modulations, only the average frequency is observed by the absorption spectra. This phenomenon is known as *motional narrowing* [12, 15].

In the liquid phase, a wide variety of inter- and intramolecular interactions occur simultaneously, e.g., the hydrogen-bond geometries of water are modulated on a fast sub-100 fs time scale whereas the hydrogen-bond lifetimes are in the range of 1–2 ps. If the frequency fluctuation correlation function is written as a superposition of a very fast and a very slow process, the infrared absorption profile has a Voigt shape. Often, a clear separation of time scales and a classification of infinitely fast and slow frequency modulations as discussed above is not possible. Accordingly, infrared lineshapes are insufficient to monitor the processes leading to frequency fluctuations on ultrafast time scales. Femtosecond infrared pulses allow for taking snap shots of instantaneous frequency distributions, providing the opportunity to follow the change of vibrational frequencies—a process called *spectral diffusion*. It will be shown in Sect. 2.2.1.2 how multidimensional, nonlinear time-resolved vibrational spectroscopies trace frequency fluctuations in real time, making them ideal tools to probe molecular dynamics.

2.1.3 Vibrational Relaxation

In time-resolved vibrational spectroscopy infrared pulses transiently generate non-equilibrium populations of vibrationally excited states. Energy relaxation to the weakly coupled bath modes brings the system back to thermal equilibrium. Often, a distinction is drawn between intra- and intermolecular relaxation pathways. While the former pathways involve other intramolecular vibrations or rotations and translations of the excited molecules, the latter pathways facilitate energy transfer to surrounding molecules. The associated vibrational lifetimes determine, for instance, the rate of chemical reactions and the relative amount of energy accepted by the solute and the solvent.

The rate of vibrational relaxation can be estimated with the help of Fermi's Golden Rule if the system-bath interaction represents a small perturbation (e.g., of a high frequency vibration with a transition frequency $\gg kT/\hbar \approx 200 \text{ cm}^{-1}$ at room temperature) [16, 17]. If we consider a vibrational degree of freedom that relaxes from $|i\rangle$ to $|j\rangle$ with $E_i - E_j = \hbar\omega_{ij} > 0$ (e.g., from the first excited state to the ground state) and denote the bath states with Greek letters ($|\alpha\rangle, |\beta\rangle, \dots$) the transition rate W_{ij} is given by:

$$W_{ij} = \frac{2\pi}{\hbar} \sum_{\alpha, \beta} \rho_{\alpha} |V_{i\alpha, j\beta}|^2 \delta(E_i - E_j + E_{\alpha} - E_{\beta}) \quad (2.24)$$

$V_{i\alpha,j\beta}$ is the coupling matrix element between the initial $|i\alpha\rangle$ and final $|j\beta\rangle$ states of the whole system and ρ_α denotes the initial distribution of bath states which is a Boltzmann distribution for a bath in thermal equilibrium: $\rho_\alpha \propto \exp(-E_\alpha/(kT))$. The delta-function ensures energy conservation, i.e., excess energy of the initially excited vibration must be accepted by the bath modes. Using the Fourier representation of the delta-function the relaxation rate becomes:

$$W_{ij}(\omega_{ij}) = \frac{1}{\hbar^2} \int_{-\infty}^{\infty} dt e^{-i\omega_{ij}t} \langle V_{ij}(t) V_{ji}(0) \rangle_B \quad (2.25)$$

Here, the time evolution of $V_{ij}(t) = \exp(i H_B t / \hbar) V_{ij} \exp(-i H_B t / \hbar)$ is determined by the bath Hamiltonian and $\langle \rangle_B$ stands for the average over the bath degrees of freedom. Equation 2.25 illustrates that besides a strong system-bath coupling V_{ij} the Fourier-amplitude of the fluctuations at the transition frequency contributes significantly to the relaxation rates.

If the bath is in thermal equilibrium, (downhill) energy relaxation should be the most probable process with $W_{ji} = \exp(-\hbar\omega_{ij}/(kT)) W_{ij}$ (cf. Eq. 2.24) leading to an irreversible vibrational population decay. This detailed-balance condition is not fulfilled by Eq. 2.25 but regained by writing the correlation function in terms of a symmetrized anticommutator $[V_{ij}(t), V_{ji}(0)]_+$ [18]:

$$W_{ij}(\omega_{ij}) = \frac{2}{\hbar^2 \left(1 + \exp\left(-\frac{\hbar\omega_{ij}}{kT}\right)\right)} \int_{-\infty}^{\infty} dt e^{-i\omega_{ij}t} \left\langle \frac{1}{2} [V_{ij}(t), V_{ji}(0)]_+ \right\rangle_B \quad (2.26)$$

It should be mentioned that here the relaxation rates are calculated from quantum-mechanical expectation values. However, theoretical correlation functions are mostly obtained from (semi-)classical molecular dynamics simulations which usually overestimate vibrational lifetimes [19, 20]. In order to improve the agreement between theory and experiment, additional quantum correction factors must be added to Eq. 2.26.

2.1.4 Molecular Vibrations as Local Probes in Hydrogen-Bonded Systems

Broadband steady state (linear) vibrational absorption spectra are routinely measured by Fourier transform infrared (FT IR) spectroscopy without relying on dispersive optics. Figure 2.2 is a collection of such spectra demonstrating the sensitivity of molecular vibrations to inter- and intramolecular interactions. The absorption of air in the range between 1000 and 4000 cm^{-1} is dominated by the two water stretching modes around 3750 cm^{-1} , the water bending mode around 1600 cm^{-1} and the anti-symmetric CO_2 stretching mode at 2400 cm^{-1} . Broad bands with individual narrow peaks exhibiting $\approx 1 \text{ cm}^{-1}$ linewidths are caused by the Franck-Condon progression

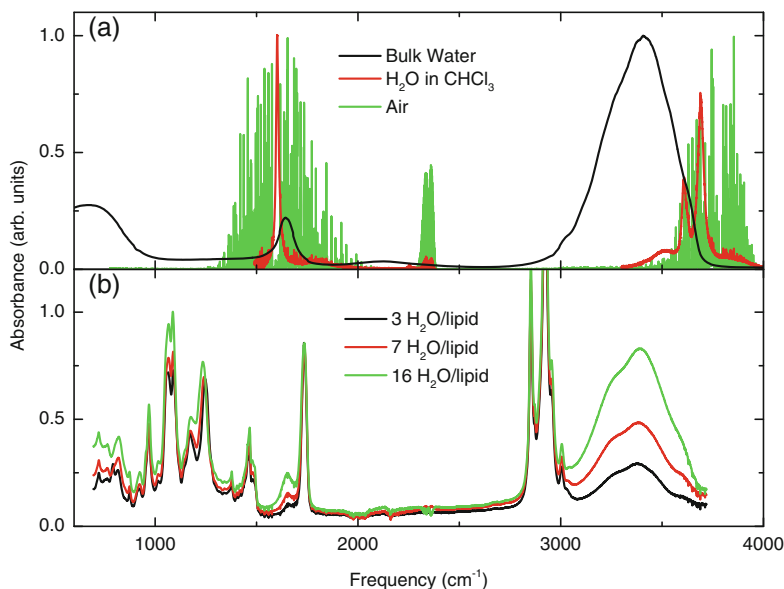


Fig. 2.2 Linear spectra of different water-containing systems. **a** FT IR spectra of bulk water forming intermolecular hydrogen bonds, water monomers in CHCl₃ solution and air demonstrating the spectral shifts of OH stretching and bending vibrations upon formation of hydrogen bonds that is accompanied by spectral broadening and changes of the transition dipole moments. **b** FT IR attenuated total reflectance spectrum of phospholipid films at different hydration levels. OH stretching and bending vibrations are clearly recognized by rising features as the water content is increased. Additional vibrational bands are the lipid marker modes

of rotational modes [21]. Rotational effects are much less pronounced for water monomers in a nonpolar solution. However, additional line broadening, e.g., due to the fluctuating solvent and decreased vibrational lifetime leads to the observation of increased linewidths compared to the individual gas phase peaks. The formation of a highly fluctuating hydrogen-bond network with a heterogeneous distribution of hydrogen-bond lengths and geometries in bulk water gives rise to broad infrared absorption spectra. Intermolecular hydrogen bonds modify the intramolecular potential energy surface in a way that the force constant of the stretching vibrations is decreased whereas it increases for the bending vibration. As a result, there is a red-shift of OH stretching frequencies and blueshift of OH bending frequencies compared to the monomers. Such shifts are generally found in hydrogen-bonded systems with a magnitude that correlates with the hydrogen-bond length [22]. Typically, the red-shift of OH stretching spectra is accompanied by an increase of the transition dipole moment [23]. Rotations of water molecules in the bulk phase are hindered due to the finite lifetime of hydrogen bonds. Therefore, librations around the three molecular axes represent the intermolecular vibrations with the highest frequencies (centered around 700 cm⁻¹).

Due to the variety of functional groups in a phospholipid molecule, the infrared absorption spectrum is rich of characteristic marker modes corresponding to different positions in the molecule. Figure 2.2b shows the FT IR attenuated total reflectance spectrum of phospholipid film made from 1,2-dioleoyl-sn-glycero-3-phosphocholine (DOPC)—the same molecule that we use for the preparation of reverse micelles (cf. Sect. 2.3.4). Some of the vibrations in the fingerprint range are the choline (975 cm^{-1}), phosphate (1090 and 1250 cm^{-1}) and carbonyl stretching (1735 cm^{-1}) vibrations whose dynamics will be discussed in Chap. 3. With increasing hydration levels the infrared absorption of water vibrations grows in and provides a probe of phospholipid hydration-shell dynamics as discussed in Chap. 4.

2.2 Theoretical Description of Nonlinear Spectroscopy

Throughout this thesis we will describe light pulses as classical electromagnetic waves with electric fields $\vec{E}(\vec{r}, t)$ that propagate in space and time and satisfy the wave equation

$$\left(\nabla^2 - \frac{1}{c^2} \frac{\partial^2}{\partial t^2} \right) \vec{E}(\vec{r}, t) = \mu_0 \frac{\partial^2}{\partial t^2} \vec{P}(\vec{r}, t). \quad (2.27)$$

Here μ_0 is the vacuum permeability and $\vec{P}(\vec{r}, t)$ is the polarization as a function of space and time. In Eq. 2.27 the polarization acts as a source for the electric field. Spectroscopy is the study of material properties by measuring the modulation of a light field due to light-matter interactions that create a polarization which in turn causes a new signal field $E_{sig}(\vec{r}, t)$ to be emitted:

$$E_{sig}(\vec{r}, t) \propto i P(\vec{r}, t) \quad (2.28)$$

Calculating $\vec{P}(\vec{r}, t)$ is thus a primary goal for theoretical descriptions of spectroscopy. The macroscopic polarization of a medium is directly connected to its microscopic dipole moments $\vec{\mu}$ by

$$\vec{P}(\vec{r}, t) \propto \langle \vec{\mu}(t) \rangle \quad (2.29)$$

with $\langle \rangle$ representing the ensemble average over all dipole moments. Changes in the expectation value $\langle \mu \rangle$ lead to a characteristic time-dependence of $\vec{P}(\vec{r}, t)$. The goal of mid-infrared spectroscopy in particular is to measure the emitted electric fields to gather microscopic information about the structure and dynamics of condensed phase molecular systems which are directly reflected by molecular vibrations.

In order to calculate the polarization in Eq. 2.29, a quantum statistical description of an ensemble of molecular dipoles interacting with an electric field is required. Often, a density matrix formalism combined with a perturbative expansion in terms

of electric fields is used to treat the light-matter interaction on a semiclassical level. A comprehensive formulation of this theory of nonlinear optical spectroscopy was developed by Mukamel [24]. Aspects of two-dimensional spectroscopy are covered by other textbooks [4, 25]. In the following, basic concepts of nonlinear spectroscopy based on the references mentioned above will be introduced.

2.2.1 Density Matrix Approach for Calculating Nonlinear Response Functions

Condensed-phase systems as investigated in this thesis consist of statistical ensembles. The density matrix ρ helps in describing such systems, e.g., the polarization as expectation value of the dipole operator $\vec{\mu}$ is obtained by evaluating the trace:

$$\vec{P}(t) = Tr [\vec{\mu}\rho(t)] \equiv \langle \vec{\mu}\rho(t) \rangle \quad (2.30)$$

The time evolution of a quantum system is determined by its Hamiltonian H , e.g., the interaction of a molecular dipole with an external electric field is described by

$$H(t) = H_0 + H_1(t) \quad (2.31)$$

$$H_1(t) = -\vec{\mu} \cdot \vec{E}(t) \quad (2.32)$$

where H_0 is the (time-independent) Hamiltonian of the unperturbed system and $H_1(t)$ accounts for the external perturbation due to the interaction of the molecular dipole operator $\vec{\mu}$ with an external electric field $\vec{E}(t)$. We assume that the solution of the time-independent Schrödinger equation for H_0 and therefore the density matrix before the interaction is known. The time evolution of the density matrix follows from the Liouville-von Neumann equation

$$\frac{d}{dt}\rho(t) = -\frac{i}{\hbar} [H, \rho(t)] \quad (2.33)$$

from which the polarization (Eq. 2.30) can be calculated. Consider a two-level system with the energy levels E_0 and E_1 that define the transition energy $E_{01} = E_1 - E_0 = \hbar\omega_{01}$. Then we get the following equations of motion for the matrix elements of ρ

$$\dot{\rho}_{00} = -i/\hbar (H_{1,01}\rho_{10} - \rho_{01}H_{1,10}) + \rho_{11}/T_1 \quad (2.34)$$

$$\dot{\rho}_{11} = -i/\hbar (H_{1,10}\rho_{01} - \rho_{10}H_{1,01}) - \rho_{11}/T_1 \quad (2.35)$$

$$\dot{\rho}_{01} = +i\omega_{01}\rho_{01} + i/\hbar H_{1,01}(\rho_{00} - \rho_{11}) - \rho_{01}/T_2 = \dot{\rho}_{10}^* \quad (2.36)$$

representing one form of the optical Bloch equations [26]. Here the last terms are phenomenologically added decay terms. That is, a non-equilibrium population inversion ($\rho_{11} - \rho_{00}$) described by the diagonal elements will decay to its equilibrium

value with the T_1 lifetime of the excited state if external perturbations are absent. Coherences described by the off-diagonal elements ρ_{ij} ($i \neq j$) oscillate at the transition frequency $\pm\omega_{01}$ and decay with the characteristic dephasing time T_2 . Since population relaxation destroys the phase relationship between coherent oscillators, it contributes to the dephasing time:

$$\frac{1}{T_2} = \frac{1}{T_2^*} + \frac{1}{2T_1} \quad (2.37)$$

Here, T_2^* is the pure dephasing time caused, e.g., by fluctuations of the solvent (cf. Eq. 2.17). So far we have neglected the influence of the perturbation Hamiltonian H_1 , which is insufficient to understand light-matter interactions as the basis for all types of spectroscopy.

In order to treat the effect of a time-dependent external perturbation, it is helpful to switch from the Schrödinger to the interaction picture. Operators in the interaction pictures (denoted by an index I) are defined as

$$A_I(t) = e^{+i/\hbar H_0(t-t_0)} A(t) e^{-i/\hbar H_0(t-t_0)} \quad (2.38)$$

and the Liouville-von Neumann equation reads:

$$\frac{d}{dt} \rho_I(t) = -\frac{i}{\hbar} [H_{1I}(t), \rho_I(t)] \quad (2.39)$$

The advantage of switching to the interaction picture is that now the time evolution is solely determined by the interaction Hamiltonian H_1 . Equation 2.39 is solved by formal integration and iterative solution:

$$\rho_I(t) = \rho_I(t_0) - \frac{i}{\hbar} \int_{t_0}^t d\tau [H_{1I}(\tau), \rho_I(t)] \quad (2.40)$$

$$\rho_I(t) = \rho_I(t_0) + \sum_{n=0}^{\infty} \rho_I^{(n)}(t) \quad (2.41)$$

$$\begin{aligned} \rho_I^{(n)}(t) = & \left(-\frac{i}{\hbar}\right)^n \int_{t_0}^t d\tau_n \int_{t_0}^{\tau_n} d\tau_{n-1} \dots \int_{t_0}^{\tau_2} d\tau_1 \\ & [H_{1I}(\tau_n), [H_{1I}(\tau_{n-1}), [\dots, [H_{1I}(\tau_1), \rho_I(t_0)] \dots]]] \end{aligned} \quad (2.42)$$

Inserting Eq. 2.32 into 2.42 and sending $t_0 \rightarrow -\infty$ the n th-order polarization $P^{(n)}(t) = \langle \mu_I(t) \rho_I^{(n)}(t) \rangle$ becomes:

$$\begin{aligned} P^{(n)}(t) \propto & -\left(-\frac{i}{\hbar}\right)^n \int_{-\infty}^t d\tau_n \int_{-\infty}^{\tau_n} d\tau_{n-1} \dots \int_{-\infty}^{\tau_2} d\tau_1 E(\tau_n) \cdot E(\tau_{n-1}) \dots E(\tau_1) \\ & \langle \mu(t) [\mu(\tau_n), [\mu(\tau_{n-1}), [\dots, [\mu(\tau_1), \rho(-\infty)] \dots]]] \rangle \end{aligned} \quad (2.43)$$

Here we discarded the subscript I and the interaction picture is indicated by the time-dependence of $\mu(t)$. Changing the integration variables to time intervals ($\tau_1 = 0$, $t_1 = \tau_2 - \tau_1$, $t_2 = \tau_3 - \tau_2$, \dots , $t_n = t - \tau_n$), one obtains the n th-order nonlinear polarization as a convolution of n electric fields with the n th-order response function $R^{(n)}(t_n, t_{n-1}, \dots, t_1)$:

$$P^{(n)}(t) \propto \int_0^\infty dt_n \int_0^\infty dt_{n-1} \dots \int_0^\infty dt_1 E(t - t_n) E(t - t_n - t_{n-1}) \dots E(t - t_n - t_{n-1} - \dots - t_1) R^{(n)}(t_n, t_{n-1}, \dots, t_1) \quad (2.44)$$

where

$$R^{(n)}(t_n, t_{n-1}, \dots, t_1) = - \left(-\frac{i}{\hbar} \right)^n \langle \mu(t_n + t_{n-1} + \dots + t_1) [\mu(t_n), [\mu(t_{n-1}), [\dots, [\mu(t_1), \rho(-\infty)] \dots]]] \rangle \quad (2.45)$$

Equation 2.45 has an intuitive physical interpretation. Each commutator represents a field-matter interaction at time t_i caused by the action of the dipole operator $\mu(t_i)$ on the density matrix. The number of commutators determines the number of field interactions and is directly related to linear and nonlinear experiments. To introduce the effects of the dipole operator interacting with the density matrix, we will first describe the linear (first-order) response before evaluating the third-order response functions that are necessary to describe 2D IR and pump-probe experiments.

2.2.1.1 Linear Response: Free Induction Decay and Absorption

The first-order nonlinear response function $R^{(1)}(t)$ according to Eq. 2.45 reads:

$$R^{(1)}(t) = i/\hbar \langle \mu(t) \mu(0) \rho(-\infty) - \mu(t) \rho(-\infty) \mu(0) \rangle \quad (2.46)$$

That is, the dipole operator $\mu(0)$ acts on the density matrix from the left (on the ket) in the first term and from the right (on the bra) in the second one. For example, consider a two-level system without permanent dipoles and a transition dipole moment of μ_{01} . If the system is in the ground state before a laser pulse arrives, the density matrix and the dipole operator are given by:

$$\rho(-\infty) = \begin{pmatrix} 1 & 0 \\ 0 & 0 \end{pmatrix} = |0\rangle \langle 0|, \quad \mu = \mu_{01} \begin{pmatrix} 0 & 1 \\ 1 & 0 \end{pmatrix} = \mu_{01} (|0\rangle \langle 1| + |1\rangle \langle 0|) \quad (2.47)$$

Evaluating the corresponding products in Eq. 2.46, we find that the two terms generate different off-diagonal elements of the density matrix: $\mu(0) \rho(-\infty) \propto \mu_{01} |1\rangle \langle 0|$, $\rho(-\infty) \mu(0) \propto \mu_{01} |0\rangle \langle 1|$. Their time evolution $e^{-i\omega_{01}t} e^{-t/T_2}$ and $e^{+i\omega_{01}t} e^{-t/T_2}$ is obtained by integrating Eq. 2.36. The multiplication with $\mu(t)$ in Eq. 2.46 corresponds

to an emission process and brings the system back to its ground state so that the response function reads:

$$R^{(1)}(t) = i/\hbar\mu_{01}^2 \left(e^{-i\omega_{01}t} - e^{+i\omega_{01}t} \right) e^{-t/T_2} \propto \sin(\omega_{01}t) e^{-t/T_2} \quad (2.48)$$

The first-order polarization is obtained by assuming a real electric field of the laser pulse:

$$E(t) = \hat{E}(t) \left(e^{-i\omega t} + e^{i\omega t} \right) = \mathcal{E}(t) + \mathcal{E}^*(t) \quad (2.49)$$

Here, $\hat{E}(t)$ is a time-dependent envelope of the field, ω is its frequency and the terms $\mathcal{E}(t)$, $\mathcal{E}^*(t)$ represent the positive and negative-frequency contribution to the total electric field $E(t)$. In vibrational spectroscopy, the resonance condition $\omega = \omega_{01}$ is usually fulfilled. Substituting this ansatz together with Eq. 2.48 into Eq. 2.44, we find that two terms oscillate with a frequency of $\pm 2\omega_{01}$ so that the integral is small compared to the slowly varying terms. In neglecting these contributions, the rotating wave approximation is applied.

The result of the preceding paragraphs is often illustrated by double-sided Feynman diagrams (Fig. 2.3) that can also be generalized to higher-order responses and lead to a convenient way of calculating nonlinear response functions. Time evolves from the bottom to the top and the current state of the density matrix is indicated. Field interactions are depicted by solid arrows. Interactions with the positive-frequency and negative-frequency part of the electric field (\mathcal{E} and \mathcal{E}^*) are depicted by arrows pointing to the right and to the left, respectively. Furthermore, dashed arrows are used to visualize the multiplication with the dipole operator that is not part of the commutators. Each field interaction produces a factor $-i/\hbar$ and each interaction from the right causes a factor of -1 (due to the commutators).

When the response functions are known, the polarization (Eq. 2.44) can be calculated and the emitted electric field follows from Eq. 2.28. An approximation frequently used is the semi-impulsive limit in which the pulses are short compared to vibrational dynamics but long compared to the oscillation period of the light field so that $\hat{E}(t) = \hat{E}\delta(t)$ (with the Dirac delta function $\delta(t)$). In this case, the polarization is directly proportional to the response function. For example, the first term in Eq. 2.48 generates a polarization that oscillates at the frequency $+\omega_{01}$ acting as a source for an

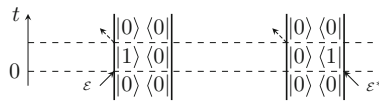


Fig. 2.3 Double-sided Feynman diagrams for the first-order response function. The *left hand side* diagram corresponds to the first term in Eq. 2.46 interacting with the positive-frequency part of the electric field whereas the *right hand side* diagram shows the second term interacting with the negative-frequency part of the electric field

electric field that is π -phase shifted with respect to the driving light field. Absorption is therefore caused by a destructive interference between the incident field and the emitted field originating from the so-called free induction decay. It should be noted that the second diagram is just the complex conjugate of the first one and therefore does not carry additional information.

In Eq. 2.48, dephasing is incorporated phenomenologically by the decay term e^{-t/T_2} . The dephasing is a result of fluctuating transition frequencies due to the interaction with a bath as discussed in Sect. 2.1.2. Assuming that the fluctuations define the instantaneous frequency ($\omega_{01}(t) = \omega_{01} + \delta\omega_{01}(t)$) and taking the ensemble average gives:

$$\begin{aligned} |0\rangle\langle 1| &= \rho_{01}(t) \propto \left\langle \exp\left(-i \int_0^t \omega_{01}(t') dt'\right) \right\rangle \\ &= e^{-i\omega_{01}t} \left\langle \exp\left(-i \int_0^t \delta\omega_{01}(t') dt'\right) \right\rangle \end{aligned} \quad (2.50)$$

This result is equivalent to Eq. 2.17. That is, applying the cumulant expansion we get the infrared absorption profile as Fourier transform of an exponential of the lineshape function (Eq. 2.19):

$$A(\omega) \propto \Re \left(i \int P^{(1)}(t) e^{i\omega t} dt \right) \propto \mu_{01}^2 \Re \left(\int e^{i(\omega - \omega_{01})t - g(t)} dt \right) \quad (2.51)$$

$g(t)$ is directly related to the frequency fluctuation correlation function $C(t)$. $C(t)$ contains information about the system-bath interaction and is one of the key quantities to be measured with vibrational spectroscopy. However, extracting the frequency fluctuation correlation function would require the impossible operation of inverting Eq. 2.51. Additionally, lineshape fitting by assuming an analytical form of $C(t)$ is often misleading because of the congested nature of condensed-phase linear absorption spectra e.g., due to the different time scales of the processes involved that lead to frequency modulations. The next section will show how third-order spectroscopy helps in revealing different line broadening contributions more reliably.

2.2.1.2 Third-Order Nonlinear Response: Four-Wave Mixing

For symmetry reasons, even-order nonlinear response functions vanish in isotropic media. Therefore, the lowest-order nonlinearity in liquid molecular systems is usually described by the third-order response function $R^{(3)}$ that is responsible for so-called four-wave mixing processes. In such processes three field interactions occur with the laser field:

$$E(t) = \hat{E}_1(t) e^{i(\vec{k}_1 \vec{r} - \omega_1 t + \Phi_1)} + \hat{E}_2(t) e^{i(\vec{k}_2 \vec{r} - \omega_2 t + \Phi_2)} + \hat{E}_3(t) e^{i(\vec{k}_3 \vec{r} - \omega_3 t + \Phi_3)} + c.c. \quad (2.52)$$

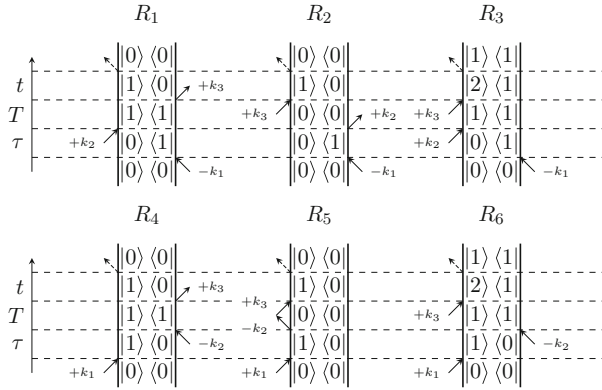


Fig. 2.4 Double-sided Feynman diagrams for the third-order response functions for the rephasing $(-\vec{k}_1 + \vec{k}_2 + \vec{k}_3)$ and non-rephasing $(+\vec{k}_1 - \vec{k}_2 + \vec{k}_3)$ phase-matching conditions

Here, \hat{E}_i , \vec{k}_i , ω_i and Φ_i are the field envelopes, wave vectors, frequencies and phases of the i th laser field, respectively. Since energy and momentum conservation must be obeyed, the conditions $\omega_{sig} = \pm\omega_1 \pm \omega_2 \pm \omega_3$ and $\vec{k}_{sig} = \pm\vec{k}_1 \pm \vec{k}_2 \pm \vec{k}_3$ (phase matching) must be fulfilled for the signal's frequency and wave vector. The signs depend on the phases of the electric fields involved. A straightforward generalization of the formalism developed in the previous section leads to the six third-order Feynman diagrams for the phase matching directions $\vec{k}_{sig} = \mp\vec{k}_1 \pm \vec{k}_2 + \vec{k}_3$ shown in Fig. 2.4 where the phase of the electric field is indicated by its wave vector. Similar to the linear response, terms that do not survive the rotating wave approximation as well as the complex conjugates that do not carry additional information are neglected.

Figure 2.5 schematically depicts the pulse sequence connected with these diagrams. The first pulse generates a coherence. As in the linear response, dephasing leads to a decay of the off-diagonal density matrix elements in the form of a free induction decay. After the *coherence time* τ , a second pulse prepares the system in a population state. During the *population time* T , the system evolves freely before the third pulse generates a coherence again. The resulting polarization is the source for the emitted signal field. Four-wave mixing is often illustrated by noticing that the first two pulses of the sequence generate a holographic population and frequency grating from which the third pulse is diffracted off [27, 28]. Population relaxation and spectral diffusion wash out the grating so that the two processes can be studied by varying the population time.

Note that the time evolution during the coherence times carries different signs for R_1 – R_3 compared to R_4 – R_6 , e.g.:

$$R_1(\tau, T, t) = -(-i/\hbar)^3 \left\langle \mu_{01}^4 e^{+i\omega_{01}\tau} e^{-\tau/T_2} e^{-T/T_1} e^{-i\omega_{01}t} e^{-t/T_2} \right\rangle \propto \left\langle e^{-i\omega_{01}(t-\tau)} \right\rangle \quad (2.53)$$

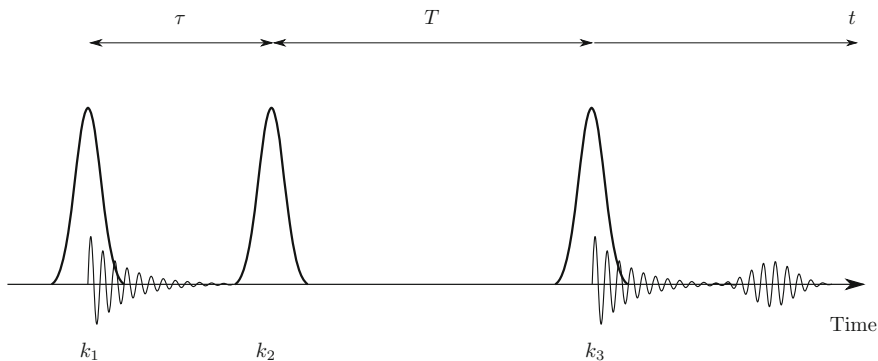


Fig. 2.5 Pulse sequence for the generation of a third-order nonlinear polarization. The first pulse creates a coherence that decays with a characteristic dephasing time. A second pulse creates a population state after the coherence time τ . After the population time T , the third pulse creates a coherence again and the resulting third-order nonlinear polarization is the source for the emitted signal field. The linear polarization after the first field interaction and nonlinear polarization after the third field interaction are schematically shown as oscillating lines

$$R_4(\tau, T, t) = -(-i/\hbar)^3 \left\langle \mu_{01}^4 e^{-i\omega_{01}\tau} e^{-\tau/T_2} e^{-T/T_1} e^{-i\omega_{01}t} e^{-t/T_2} \right\rangle \propto \left\langle e^{-i\omega_{01}(t+\tau)} \right\rangle \quad (2.54)$$

In the case of inhomogeneous broadening, diagrams R_1 – R_3 cause a macroscopic polarization at $t = \tau$ that will emit a signal field after the free induction decay—a phenomenon called photon echo. R_1 – R_3 are therefore referred to as *rephasing* Feynman diagrams while R_4 – R_6 are the *non-rephasing* diagrams.

R_1 and R_4 are in the $v = 1$ state after the second field interaction whereas R_2 and R_5 are in the ground state. Although their evolution during the population is the same, the origin of the signal is different with the former being caused by the stimulated emission from the $v = 1$ state and the latter stemming from the ground state bleach. Both contributions appear at the same spectral positions. Diagrams R_3 and R_6 are in a $|2\rangle \langle 1|$ -coherence after the third field interaction, therefore sensitive to the $v = 1$ to 2 absorption that is red-shifted due to the anharmonicity of condensed-phase molecular vibrations. Note that only one field interaction from the right occurs so that these diagrams generate signals with an opposite sign compared to the ones discussed before.

While the stimulated emission and excited state absorption decay with the T_1 lifetime, the ground-state bleaching decay may be delayed when the excitation does not relax to the ground state $|0\rangle$ directly. Instead one often speaks of a so-called hot ground state $|0'\rangle$ where the population of anharmonically coupled low-frequency modes causes a persistent bleaching of the initially excited transition. The corresponding time-dependent amplitude maps the recovery of the original ground state, thus giving insight into the thermalization of the sample. Since the ground state bleach and excited state emission signals arise at the same frequency positions, the

time evolution of the excited state absorption is the most direct way to extract the excited state lifetime.

In order to calculate the third-order nonlinear polarization (Eq. 2.44), the ensemble average has to be evaluated. Using the cumulant expansion and the definition of the lineshape functions (Eq. 2.19), the rephasing and non-rephasing response functions take the following form:

$$R_{1,2,3}(\tau, T, t) = -2i/\hbar^3 \mu_{01}^4 \left(e^{-i\omega_{01}(t-\tau)} - e^{-i((\omega_{01}-\Delta)t-\omega_{01}\tau)} \right) e^{-(\tau+t)/(2T_1)} e^{-T/T_1} \cdot e^{-g(\tau)+g(T)-g(t)-g(\tau+T)-g(T+t)+g(\tau+T+t)} \quad (2.55)$$

$$R_{4,5,6}(\tau, T, t) = -2i/\hbar^3 \mu_{01}^4 \left(e^{-i\omega_{01}(t+\tau)} - e^{-i((\omega_{01}-\Delta)t+\omega_{01}\tau)} \right) e^{-(\tau+t)/(2T_1)} e^{-T/T_1} \cdot e^{-g(\tau)-g(T)-g(t)+g(\tau+T)+g(T+t)-g(\tau+T+t)} \quad (2.56)$$

Here we made use of the harmonic approximation for the transition dipole moments $\mu_{12} = \sqrt{2}\mu_{01}$ and introduced the anharmonicity $\Delta = \omega_{01} - \omega_{12}$; we implicitly assumed that the FFCF of the $v = 0$ to 1 is the same as that of the $v = 1$ to 2 transition. Note that from Eq. 2.47 onward we neglected the time-dependence of the dipole moment's amplitude corresponding to the Condon-approximation. The assumption is not applicable for calculations of water OH stretching lineshapes where frequency shifts due to fluctuating hydrogen-bond geometries are accompanied by changes of the transition dipole moment [29].

Two-Dimensional Infrared Spectroscopy

Measuring the response functions in its dependency of all three time delays opens the possibility of obtaining two-dimensional infrared (2D IR) spectra. Although this work concentrates on vibrational spectroscopy, most of the concepts presented in the following are applicable to 2D spectroscopy in general from the UV to the mid-infrared. One way to measure 2D spectra is depicted in Fig. 2.6a. Three pulses with

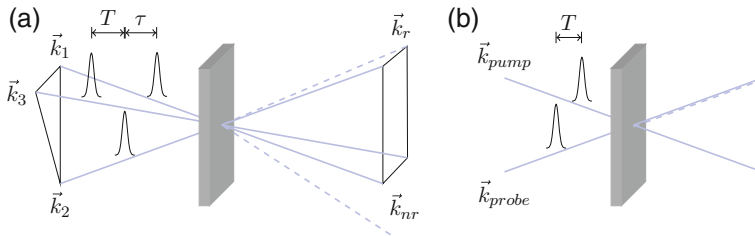


Fig. 2.6 Schematic representation of **a** two-dimensional infrared and **b** pump-probe experiments. In **a**, the coherence time τ and population time T can be varied allowing for a discrimination of the rephasing ($\vec{k}_r = -\vec{k}_1 + \vec{k}_2 + \vec{k}_3$) and non-rephasing signals ($\vec{k}_{nr} = +\vec{k}_1 - \vec{k}_2 + \vec{k}_3$). In **b**, the only free parameter is T and the signal is emitted in the direction of the probe

different wave vectors and tuneable time delays interact in the sample so that the non-linear polarization emits a signal field E_{sig} in the rephasing and non-rephasing phase matching directions $\vec{k}_r = -\vec{k}_1 + \vec{k}_2 + \vec{k}_3$ and $\vec{k}_{nr} = +\vec{k}_1 - \vec{k}_2 + \vec{k}_3$. Section 2.3.2 describes one possibility to measure E_{sig} by means of spectral interferometry. Compared to the linear case, the third-order response $R(\tau, T, t)$ contains two coherence periods (τ and t). A two-dimensional Fourier transform converts the response functions into the frequency domain so that the response functions $R(\omega_1, T, \omega_3)$ correlate the *excitation frequency* ω_1 and *detection frequency* ω_3 .

The most common way to show such correlation plots are so-called absorptive 2D spectra $S(\omega_1, T, \omega_3)$ for which the rephasing and non-rephasing terms are added [30, 31]:

$$S(\omega_1, T, \omega_3) = \Re \left\{ i \left(\sum_{n=1}^3 R_n(-\omega_1, T, \omega_3) + \sum_{n=4}^6 R_n(+\omega_1, T, \omega_3) \right) \right\} \quad (2.57)$$

Here, the semi-impulsive limit was applied. Note that the rephasing terms are evaluated as a function of $-\omega_1$ so that the positive-frequency part of the 2D spectrum is composed of rephasing and non-rephasing spectra lying in the same quadrant of the (ω_3, ω_1) -plane.

Some capabilities behind the general approach of 2D spectroscopy are illustrated in Fig. 2.7 for a system consisting of two non-interacting oscillators (ν_a, ν_b) at the frequencies ω_a and ω_b with a T_1 lifetime of 1.5 and 1.0 ps, respectively, and two different FFCFs (Fig. 2.7b). A constant was chosen for ν_a while ν_b follows a Kubo ansatz with a correlation time of 500 fs. The amplitude of both FFCFs are the same. Extracting the line broadening contributions from the linear spectra (Fig. 2.7a, calculated with Eq. 2.51) would involve a careful peak shape analysis of the partly overlapping bands.

The information content of 2D spectra for population times of 50 and 500 fs as shown in Fig. 2.7c, d and calculated with Eq. 2.57 is much larger. Both vibrations show a positive feature (yellow-red contours) along the diagonal ($\omega_1 = \omega_3$) due to the ground state bleach and excited state emission as well as a negative signal (blue contours) anharmonically red shifted with respect to the detection-frequency axis caused by the excited state absorption. The signal contributions decay with increasing T according to their lifetime. Dramatic differences are observed for the peak shapes. Since 2D spectra measure correlations between the excitation and detection frequency, their shape is dictated by the course of the FFCF. The correlation between these frequencies for inhomogeneously broadened transitions is reflected in stationary lineshapes that are elongated along the diagonal as shown for the peaks of ν_a . For non-constant FFCFs such as in the case of ν_b , a vibration's memory of its initial excitation frequency is gradually extinguished leading to round (homogeneous) 2D lineshapes on the time scale of frequency fluctuations. Generally, the diagonal width of a 2D peak reflects its total linewidth whereas the antidiagonal width is determined by the homogeneous linewidth including contributions from pure dephasing and the finite vibrational lifetime (cf. Eq. 2.37) [32, 33].

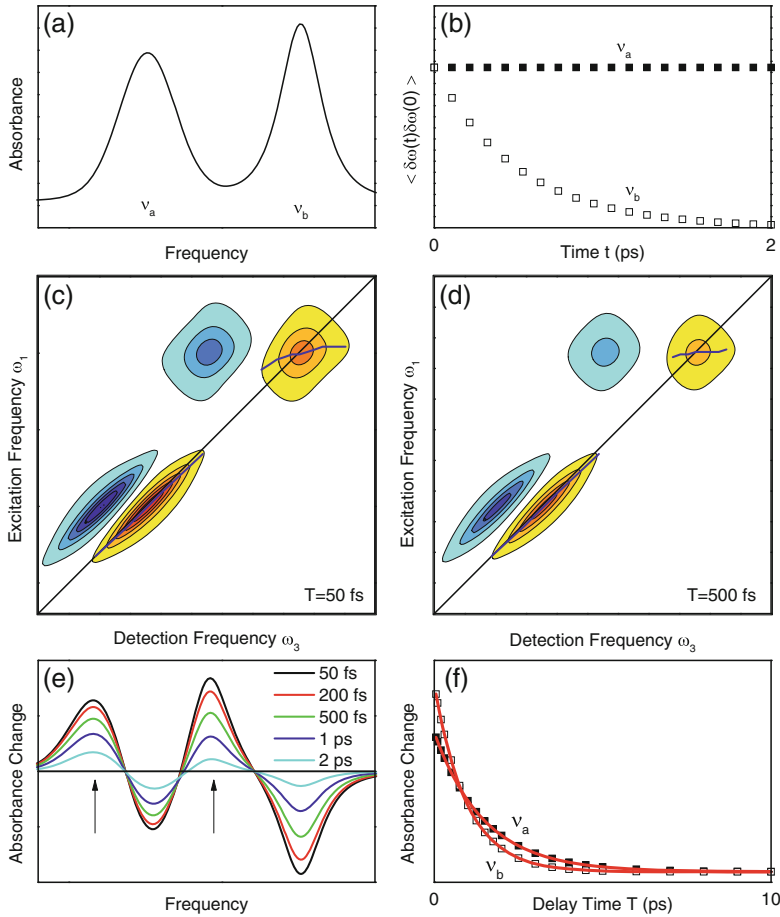


Fig. 2.7 Calculated **a** linear, **c, d** 2D, and **e** pump-probe spectra of two transitions ν_a and ν_b for a FFCF shown in **b**. Along the diagonal ($\omega_1 = \omega_3$) the 2D spectra show positive peaks (yellow, red) originating from the ground state bleach and stimulated emission. The negative excited state absorption signal (blue) is anharmonically red-shifted along the detection-frequency axis. Inhomogeneous broadening of ν_a results in spectra elongated along the diagonal whose antidiagonal width is determined by the lifetime broadening. The FFCF of ν_b decays on a 500 fs time scale leading to a reshaping its 2D spectrum. Those features are not resolved in pump-probe spectra **e** due to the integration along the excitation-frequency axis which also leads to a stronger overlap of the two signal contributions for ν_a . **f** The time evolution of the excited state absorption at the frequencies indicated by arrows in **e** reveals T_1 lifetimes of 1.5 and 1.0 ps, respectively

Frequently, center lines that are plotted as blue lines in Fig. 2.7c, d are used for a quantitative 2D lineshape analysis. They are constructed by scanning the detection-frequency axis and connecting the respective points with a maximum signal amplitude along the excitation-frequency axis. Round peak shapes originating from homogeneous lineshapes give horizontal lines with a *center line slope* (CLS) of zero. In

contrast, inhomogeneous lineshapes that are elongated along the diagonal have a CLS of 1. Plotting the CLS as a function of population time allows for a quantification of spectral reshaping rates (i.e., spectral diffusion) of 2D peaks. It is often assumed that the CLS decay or the change of the eccentricity of 2D spectra is directly proportional to the FFCF [34, 35]. This assumption is only true within a so-called short-time approximation [36] and for Gaussian frequency fluctuations. It has been shown to be invalid for some realistic systems [37, 38].

In addition to the information obtained by a lineshape analysis, 2D spectra are able to reveal anharmonic couplings between different vibrations which were briefly discussed in Sect. 2.1.1. Generally, a system of two coupled oscillators can be described in a normal-mode picture or in an exciton picture [39, 40]. In both cases, couplings give rise to an energy level scheme which contains all information about diagonal and off-diagonal anharmonicities. Off-diagonal anharmonicities cause the appearance of (off-diagonal) *cross peaks* in the 2D spectrum. For instance, a population of one vibration results in a depopulation of the common ground state, i.e., there will also be a bleach of the fundamental transition of the second vibration so that an off-diagonal signal will occur at the excitation frequency of the first and the detection frequency of the second mode. Additional signals due to absorption of combination modes cause a second contribution to the cross peaks which permits the direct observation of off-diagonal vibrational couplings.

An instantaneous response is expected if anharmonic coupling is the only mechanism leading to cross-peak signals. However, cross peaks also indicate population transfer from one mode to another. In this case, they follow a more complicated time evolution that is determined by the time constants of the initial energy transfer and the subsequent population relaxation of the energy-accepting vibration.

Pump-Probe Spectroscopy

Pump-probe spectroscopy is a special case of third-order nonlinear spectroscopy where the first two field interactions originate from the same pump pulse, i.e., $\vec{k}_1 = \vec{k}_2 = \vec{k}_{\text{pump}}$ and $\tau = 0$ (cf. Fig. 2.6b). A pump-probe signal is therefore emitted in the direction of the probe $\vec{k}_{\text{sig}} = -\vec{k}_{\text{pump}} + \vec{k}_{\text{pump}} + \vec{k}_{\text{probe}}$ so that the probe and signal fields interfere on the detector giving rise to a pump-induced *absorbance change*

$$\Delta A = -\log \left(T_{\text{sample}} / T_{\text{sample}}^{(0)} \right) \quad (2.58)$$

where T_{sample} and $T_{\text{sample}}^{(0)}$ represent the sample transmission with and without pump excitation. From an experimental point of view, pump-probe spectroscopy is easier to implement than 2D IR techniques because it involves only two beams and one time delay. The price one has to pay is that the frequency resolution along the excitation axis is lost. If the pump pulses are approximated as delta pulses with a flat spectrum, fixing $\tau = 0$ results in pump-probe spectra that are equivalent to 2D spectra integrated along the excitation-frequency axis.

Figure 2.7e shows transient pump-probe spectra as a function of the pump-probe delay time (i.e., the population time T in 2D spectra). Negative absorbance changes are caused by the ground state bleach and excited state emission pathways. The anharmonicity causes red-shifted positive signals due to the excited state absorption. Note that by convention, the sign of 2D and pump-probe signals is different. The pump-probe spectra do not offer an intuitive way of distinguishing different line broadening mechanisms. Moreover, they suffer from overlapping contributions of different signals. For example, comparison between 2D and pump-probe spectra of ν_a reveals that the latter are strongly influenced by an overlap of the ground and excited state pathways due to the pronounced inhomogeneous lineshape and the small anharmonicity. While the two signal contributions are well separated for ν_b , other overlapping pump-probe contributions occur due to the $v = 0$ to 1 transition of ν_a and the $v = 1$ to 2 transition of ν_b . Additional cancellation effects would be observed if anharmonic couplings and energy transfer between ν_a and ν_b were included in the model calculations.

If all signal contributions are well separated, the pump-probe technique offers the advantage of only having to scan one time delay to measure excited state lifetimes. An example is shown in Fig. 2.7f that shows the time evolution of the excited state absorption as a function of the pump-probe delay time (T). In agreement with the parameters put into the model, the signals fit well to monoexponential decays with time constants of 1.5 and 1.0 ps for ν_a and ν_b , respectively (red lines).

Experiments are conducted with pulses of finite duration. Therefore, a sequential interaction as assumed so far is not always fulfilled. At pulse delays shorter than the pulse duration additional field interactions occur causing spikes in the time-resolved measurements. Those artifacts, commonly referred to as *coherent pump-probe coupling*, may partly mask a molecule's response around zero delay times.

Negative delay times correspond to a situation when the probe interaction precedes the arrival of the pump pulse. As a consequence, the probe creates a coherence followed by a free induction decay that can be perturbed by the pump interactions. The corresponding pump-probe signals at negative delay times are therefore called perturbed free induction decay and can give information about dephasing properties of the system [41].

In the theoretical description of the nonlinear response, we neglected that the dipole interaction (Eq. 2.32) has the form of a dot product, i.e., Eq. 2.44 should carry a proportionality factor that depends on the relative orientation of the transition dipole and the electric field polarization at the time of each interaction. There are different mechanisms leading to a reorientation of transition dipoles between two interactions, e.g., rotation of a molecule or functional group as well as intermolecular energy transfer. It was recognized in time-resolved fluorescence [42, 43] and later applied to time-resolved vibrational spectroscopy [44] that the use of linearly polarized pulses allows for measuring the time scales of such reorientations. The idea is as follows: If a light pulse is linearly polarized along the z -axis of a Cartesian coordinate system then the interaction probability with a dipole moment is proportional to its z -component.

Expressing the dipole moment in spherical coordinates with the polar and azimuthal angles Θ and Φ , the initial normalized distribution of excited dipoles after the first two field interactions is

$$W(\Theta_0, \Phi_0) = \frac{3}{4\pi} \cos^2 \Theta_0 = \frac{3}{4\pi} (1 + P_2(\cos \Theta_0)) \quad (2.59)$$

with the second-order Legendre polynomial P_2 . The probability to find a dipole at the angles (Θ, Φ) after the time T provided that it was initially aligned at (Θ_0, Φ_0) , can be expressed in terms of spherical harmonic functions. We then calculate the probability that the signal, e.g., generated in a pump-probe experiment, is emitted parallel ($\Delta A_{||}$) or perpendicular (ΔA_{\perp}) to the excitational polarization. If the vibrational population relaxes directly to the ground state, the pump-probe signal is proportional to the probability $P_v(T)$ of a vibrational excitation to survive during the population time and we get:

$$\Delta A_{||}(T) \propto P_v(T) \left(\frac{1}{3} + \frac{4}{15} \left\langle P_2 \left[\hat{\mu}(T) \hat{\mu}(0) \right] \right\rangle \right) \quad (2.60)$$

$$\Delta A_{\perp}(T) \propto P_v(T) \left(\frac{1}{3} - \frac{2}{15} \left\langle P_2 \left[\hat{\mu}(T) \hat{\mu}(0) \right] \right\rangle \right) \quad (2.61)$$

Here $\hat{\mu}(T)$ is the unit vector in the direction of a dipole moment at time T and $\langle \rangle$ denotes the ensemble average. The *anisotropy*

$$r(T) = \frac{\Delta A_{||}(T) - \Delta A_{\perp}(T)}{\Delta A_{||}(T) + 2 \cdot \Delta A_{\perp}(T)} = \frac{2}{5} \left\langle P_2 \left[\hat{\mu}(T) \hat{\mu}(0) \right] \right\rangle \quad (2.62)$$

is therefore a direct measure of orientational relaxation. Note that the denominator that is often referred to as *isotropic absorbance change*

$$\Delta A_{iso} = \frac{1}{3} (\Delta A_{||}(T) + 2 \cdot \Delta A_{\perp}(T)) \propto P_v(T) \quad (2.63)$$

does not contain reorientational effects and is the most direct probe for vibrational relaxation. It should be mentioned that the picture of reorienting transition dipoles is only correct for direct vibrational relaxation to the ground state. If pump-probe signals are dominated by anharmonic couplings to low-frequency modes populated after intermolecular energy relaxation, the anisotropy at population times longer than the vibrational lifetime is influenced by oscillators that were not excited initially.

The control of the polarization of all pulses in a nonlinear experiment is useful to suppress or enhance certain Feynman diagrams involving vibrational transitions that are not parallel to each other. Polarization control is therefore often applied in 2D IR or higher-order spectroscopy to enhance cross peaks with respect to the diagonal ones. A detailed description is given in Chap. 5 of [4].

2.3 Experimental

2.3.1 Generation and Characterization of Short Tuneable Mid-Infrared Pulses

With Ti:sapphire as a laser gain medium [45], reliable near-infrared femtosecond lasers are fundamental tools for ultrafast spectroscopy. Amplified laser systems with kHz-repetition rates and mJ-pulse energies are now commercially available. Two different laser systems were used for the 2D IR (Coherent Micra+Elite, <40 fs pulse duration, 2.5 mJ pulse energy, 1 kHz repetition rate) and two-color pump-probe (Coherent Libra HE, 45 fs pulse duration, 3.5 mJ pulse energy, 1 kHz repetition rate) experiments presented in this thesis.

A convenient method to generate tuneable femtosecond pulses in the mid-infrared is nonlinear parametric frequency conversion [46]. Figure 2.8 depicts the experimental setup of such a frequency converter. Near-infrared 800 nm pulses (pulse energy 0.7 mJ) from an amplified laser system are split into three arms with different pulse energies. The smallest fraction of energy is used for supercontinuum generation in a sapphire plate (1 mm thickness). Signal and idler pulses with pulse energies in the sub- μ J range are obtained by optical parametric amplification of the supercontinuum in a BBO crystal (type II, $\theta = 25^\circ$, 4 mm thickness). Using the signal as a seed for a second amplification in the same BBO crystal leads to high-energy ($\approx 150 \mu$ J) signal and idler radiation. An optional third amplification with a 2 mm thick BBO yields $>250 \mu$ J. Difference frequency generation of signal and idler in GaSe (for $1000\text{--}2500 \text{ cm}^{-1}$, type II, z-cut $\theta = 14^\circ$, 0.5–1 mm thickness) or AgGaS₂ (for $2500\text{--}3500 \text{ cm}^{-1}$, type I, $\theta = 42^\circ$, 0.5–1 mm thickness) delivers intense femtosecond pulses in the mid-infrared. Pulse energies of 2 μ J with pulse durations of 70–150 fs depending on the output frequency are obtained with two amplifications, whereas a third amplification leads to 7 μ J at 50–100 fs. All parameters of the pulses used in the experiments are given in the appendix (Table A.1, p. 100).

Due to the limited response times of photodetectors, a direct measurement of the electric field of optical pulses is impossible. Therefore, a broad set of referencing techniques combined with time-integrating detectors is used for ultrashort pulse characterization. In the simplest case, a pulse is referenced with itself by a nonlinear second-order process in an autocorrelation setup [47]. For pump-probe experiments, one is interested in the time resolution of the experiment that is given by the cross-correlation of the pump and probe pulses. The time-integrated (second-order) cross-correlation signal I_{XC} reads:

$$I_{XC}(\tau) \propto \int_{-\infty}^{\infty} |E_{pump}(t) \cdot E_{probe}(t - \tau)|^2 dt = \int_{-\infty}^{\infty} I_{pump}(t) I_{probe}(t - \tau) dt \quad (2.64)$$

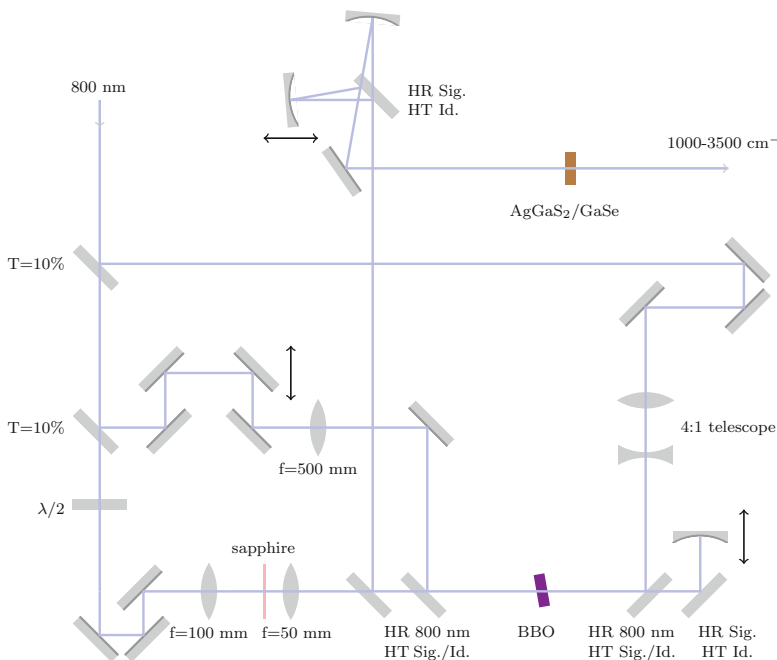


Fig. 2.8 Parametric frequency conversion for the generation of tuneable mid-infrared pulses. Weak signal and idler pulses with pulse energies $< 1 \mu\text{J}$ are generated by optical parametric amplification of a supercontinuum generated in a sapphire plate. Subsequently, the signal is recollimated and further amplified in a second pass through the amplification crystal. Difference frequency generation of signal and idler radiation with pulse energies in the range of $150 \mu\text{J}$ leads to mid-infrared pulses. Typical pulse energies exceed $2 \mu\text{J}$ and values of up to $7 \mu\text{J}$ are obtained with an optional third amplification for the signal radiation (not shown). Tuneability is achieved by changing the phase matching angle of the amplification crystal (BBO) and the difference frequency generation crystal (AgGaS_2 or GaSe). Abbreviations: T—transmission, HR/HT: dichroic mirrors optimized for high reflection/high transmission of different spectral components, Sig./Id.: signal and idler radiation with wavelengths between $1200\text{--}1600\text{ nm}$ and $1600\text{--}2400\text{ nm}$, respectively

Here $E_{\text{pump,probe}}$ and $I_{\text{pump,probe}}$ are the electric fields and intensities of the pump and probe pulses, respectively and τ is a tuneable time delay between them. The temporal width of $I_{XC}(\tau)$ is a measure of the time resolution in pump-probe experiments. Note that any phase information about the pulses is lost due to the functional form of Eq. 2.64. In some limits pulse durations can be extracted from such correlation techniques when the analytical form of the pulse envelope is known. For example, Fig. 2.9 shows a cross-correlation of pump and probe pulses with a frequency around 3000 cm^{-1} together with a Gaussian fit of 110 fs width (FWHM). Assuming that both pulses have the same spectral bandwidth and phase one extracts a pulse duration of $\approx 80\text{ fs}$. However, more sophisticated methods are necessary to retrieve the full phase information without further assumptions.

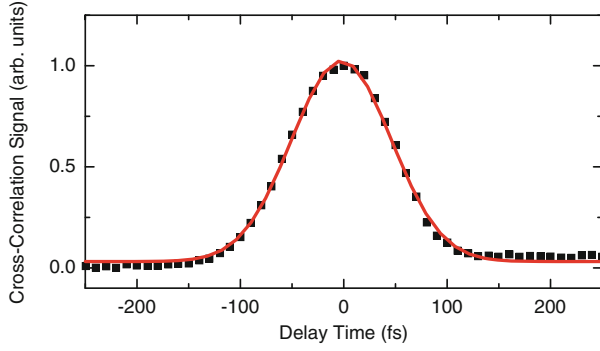


Fig. 2.9 Cross-correlation trace of pump and probe pulses centered around 3000 cm^{-1} (*squares*). The *red line* represents a Gaussian fit with a width of 110 fs (FWHM) (color figure online)

Frequency-resolved detection of auto-correlation or cross-correlation signals is an established technique well-known as frequency-resolved optical gating (FROG) [48]. Since the photon-echo setup (cf. Sect. 2.3.2) uses three pulses with independent delays in a boxcar geometry, a so-called transient grating (TG)-FROG is easily implemented. In such an arrangement, two pulses that are overlapped in space and time generate a refractive-index grating. A third pulse that is diffracted off that grating is independently delayed so that frequency-resolved and time-integrated detection leads to the TG-FROG signal:

$$I_{TG-FROG}(\omega, \tau) \propto \left| \int_{-\infty}^{\infty} E^2(t) E^*(t - \tau) e^{-i\omega t} dt \right|^2 \quad (2.65)$$

Iterative procedures are used to extract the electric field amplitude and phase of a pulse.

Another possibility is to measure a pulse phase by spectral interference with a frequency-shifted copy. This technique is referred to as spectral phase interferometry for direct electric-field reconstruction (SPIDER) [49]. A spectrometer measures the interference pattern:

$$I_{SPIDER}(\omega) = |E(\omega)|^2 + |E(\omega + \Omega)|^2 + 2 \cdot |E(\omega)| |E(\omega + \Omega)| \cos(\Phi(\omega + \Omega) - \Phi(\omega) + \omega\tau) \quad (2.66)$$

Here, $E(\omega)$ and $\Phi(\omega)$ are the spectral amplitude and phase of the electric field, Ω is the frequency shift and τ is the delay between the two pulses. $E(\omega)$ is easily obtained from the square root of the pulse spectrum so that the spectral phase can be retrieved non-iteratively by a Fourier analysis.

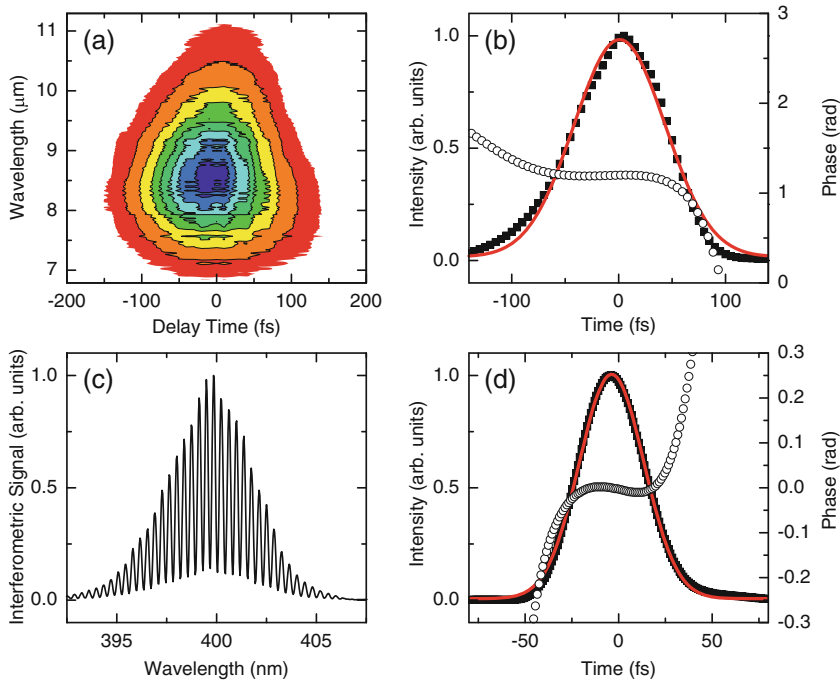


Fig. 2.10 **a** FROG trace of a pulse with a center wavelength between 8 and 9 μm that is used for photon-echo measurements in the phosphate stretching range as discussed in Sect. 3.1. **b** Retrieved intensity (*solid squares*) and phase profiles (*open circles*). A Gaussian fit (*red line*) indicates pulse durations of approximately 100 fs (FWHM). **c** SPIDER interferogram of a pulse from the amplified laser system used for the pump-probe experiments. The intensity and phase profiles for the retrieved ≈ 40 fs pulse are shown in **d** (color figure online)

Figure 2.10a, b display the FROG trace as well as the retrieved pulse used in a typical photon-echo measurement in the phosphate stretching range (cf. Sect. 3.1). Moderate distortions of the FROG trace point to slight residual third-order dispersion of the pulse. The envelope shows a width of 100 fs corresponding to about 3.6 cycles of the electric field. Pulse retrieval was facilitated by commercial software (FROG 3.2.2, Swamp Optics, LLC). For comparison, Fig. 2.10c, d show a SPIDER interferogram of a pulse derived from a typical amplified femtosecond laser system measured with a commercial LX-SPIDER (APE GmbH, [50]) and the corresponding retrieved pulse (pulse duration ≈ 40 fs).

It should be noted that none of the techniques described above is sensitive to the carrier-envelope phase, i.e., the relative phase between the oscillating electric field of a pulse and its envelope. Therefore, the task of field-resolved detection requires other methods such as free-space electro-optic sampling [51].

2.3.2 Passively Phase-Stabilized Heterodyne-Detected Photon Echo

2D IR spectroscopy can be performed by a variety of experimental setups. Pump-probe measurements with tuneable narrow-band pump pulses allow for a direct acquisition of 2D IR spectra in the frequency domain [52]. The drawback of limited (picosecond) time resolution is circumvented with coherent spectroscopy in the time domain by using three pulses with independent delays where the excitation-frequency axis is obtained by a numerical Fourier transform along the (first) coherence time delay. Using coherent techniques requires active or passive phase stabilization of the pulses involved. This task was achieved by different groups using either a non-collinear, a pump-probe or a collinear beam geometry [53–59].

Figure 2.11 shows the experimental implementation to measure 2D IR spectra used in this work based on the approach outlined in [53]. Mid-infrared pulses are split into two copies by the help of a beamsplitter. A translation stage in the beam path of one pulse allows for tuneability of the relative time delay Δt_1 . Focussing the two initially horizontally aligned pulses onto a horizontal reflective diffractive optic element (DOE) generates 4 pulses that define the corners of a rectangle (cf. Fig. 2.12a). For clarity, the four beam paths after diffraction are drawn as dashed

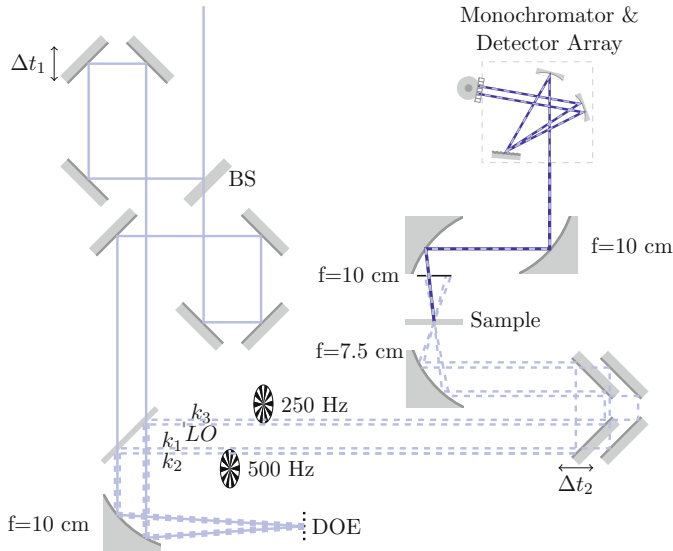
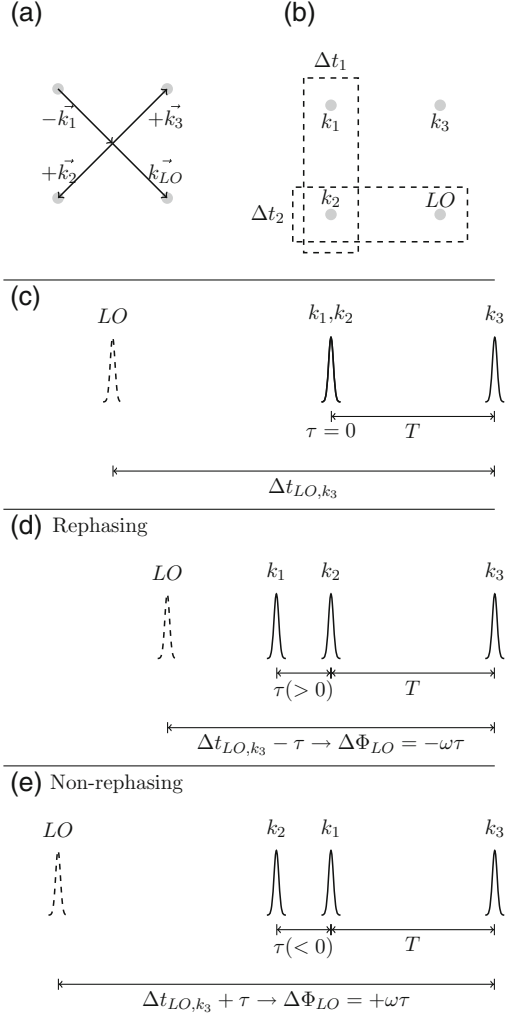


Fig. 2.11 Sketch of the photon-echo setup for measuring 2D IR spectra. Phase locked pairs of pulses are obtained by the use of a beamsplitter (BS) and a diffractive optic element (DOE). In this way, the third-order nonlinear signal (solid blue line) generated by k_1 , k_2 and k_3 is heterodyned with a local oscillator (LO) pulse and the resulting spectral interferogram is detected by a 64-pixel mercury cadmium telluride detector array. Translation stages allow for independent tuning of the two delay times between the signal-generating beams

Fig. 2.12 **a** Phase matching geometry used for photon echo experiments. The local oscillator is automatically aligned collinearly with the emitted third-order signal ($\vec{k}_{signal} = -\vec{k}_1 + \vec{k}_2 + \vec{k}_3 = \vec{k}_{LO}$). **b** Schematic plot of the correlated delays used in the experimental setup (Fig. 2.11). The second delay Δt_2 sets τ . The first delay Δt_1 corresponds to T only if $\tau < 0$ (k_2 precedes k_1). In case of $\tau > 0$, $\Delta t_1 = T - \tau$ so that the first delay has to correct for τ to ensure a constant T . **c–e** show the corresponding pulse sequences and the resulting variable time delay of the local oscillator that leads to measurements in the rotating frame with respect to the coherence time τ . For details see text



lines in Fig. 2.11. The lower two beams (k_2 , LO) experience a second time delay Δt_2 with respect to the upper ones (k_1 , k_3). After being focussed into the sample, k_1 , k_2 and k_3 generate a third-order nonlinear signal in the (rephasing) phase matching direction $\vec{k}_{signal} = -\vec{k}_1 + \vec{k}_2 + \vec{k}_3 = \vec{k}_{LO}$ so that the signal and local oscillator pulses propagate collinearly (cf. Fig. 2.12a). The focal spot size is about 100 and 200 μm at 3000 and 1250 cm^{-1} , respectively, and each pulse has an energy on the order of 1 μJ . In order to avoid signals generated by the local oscillator, it is attenuated by a copper mesh (OD = 2) and advanced in time by inserting 0.5 mm ZnSe into the k_3 beam path. The spectral interference pattern between the signal and local oscillator

$$I_{2DIR}(\omega_{Det}) = |E_{LO}(\omega_{Det}) + E_{signal}(\omega_{Det})|^2 \quad (2.67)$$

is then measured as a function of the detection frequency ω_{Det} with a monochromator and a 64-pixel mercury cadmium telluride (MCT) detector array. Here, E_{LO} and E_{signal} are the local oscillator and signal electric fields, respectively.

Assuming that the signal fields are small compared to the local oscillator one obtains:

$$I_{2DIR}(\omega_{Det}) = |E_{LO}(\omega_{Det})|^2 + 2\Re(E_{LO}^*(\omega_{Det})E_{signal}(\omega_{Det})) \\ |E_{LO}(\omega_{Det})|^2 + 2|E_{LO}(\omega_{Det})||E_{signal}(\omega_{Det})| \cdot \cos(\Phi_{signal} - \Phi_{LO}) \quad (2.68)$$

$|E_{LO}(\omega)|^2$ is the local oscillator spectrum. It is subtracted by chopping one of the signal generating beams at a 500Hz rate (here: k_2) and taking the differential signal between two consecutive pulses. In principle, a scattering contribution to the measured signal originating from scattering of the sample and the sample-cuvette windows cannot be excluded. This contribution is eliminated by an optional second chopper for k_3 running at 250Hz and thereby allowing for subtraction of the k_2 -scattering.

The phase difference in Eq. 2.68 can be written as

$$\Phi_{signal} - \Phi_{LO} = (-\Phi_1 + \Phi_2) + (\Phi_3 - \Phi_{LO}) + \phi_{signal} \\ = (-\Phi_1 + \Phi_3) + (\Phi_2 - \Phi_{LO}) + \phi_{signal} \quad (2.69)$$

where $\Phi_{1,2,3,LO}$ are the phases of k_1, k_2, k_3 and k_{LO} , respectively and ϕ_{signal} is the phase related to a system's nonlinear response function. An important consequence of using the DOE is that the setup is inherently phase stabilized because it produces phase locked pairs of pulses. Before the DOE, phase differences between k_1 and k_2 as well as k_3 and k_{LO} cancel out (cf. first line in Eq. 2.69). After the DOE, phase fluctuations cancel out because there are similar beam paths for the pairs (k_1, k_3) and (k_2, k_{LO}) (second line in Eq. 2.69).

Note that E_{signal} and I_{2DIR} intrinsically carry a time-dependence with respect to Δt_1 and Δt_2 . As depicted in Fig. 2.12b, the first delay moves (k_1, k_2) with respect to (k_3, k_{LO}) whereas the second moves (k_2, k_{LO}) with respect to (k_1, k_3) . Δt_2 moves are directly connected to the coherence time τ . Positive values of τ scan the rephasing signal contributions. $\tau < 0$ corresponds to a change of the (k_1, k_2) time-ordering so that the non-rephasing signal is measured as a function of $-\tau$. For the non-rephasing diagrams, Δt_1 defines the population time T . Since Δt_2 moves k_2 relative to k_3 , Δt_1 has to be moved accordingly to ensure a constant population time T for the rephasing diagrams.

An interesting consequence of the correlated time delays is that the local oscillator moves in time as a function of τ (Fig. 2.12c–e). While the relative phase shift for rephasing diagrams (Fig. 2.12d) equals $-\omega\tau$ because the local oscillator approaches k_3 , a relative phase shift of $+\omega\tau$ occurs for the non-rephasing diagrams when the local oscillator is shifted away from k_3 . Consequently, the τ -dependence in the third-order response functions (Eqs. 2.55, 2.56) cancels out so that the spectral interferogram is

free from oscillations in τ . This is equivalent to projecting the 2D spectrum onto $\nu_1 = 0$. Correct spectra are obtained by multiplying the proper phase factors in the analysis procedure. The advantage over a fixed $k_3 - k_{LO}$ time difference is that according to the Nyquist-Shannon sampling theorem [60], the coherence time step determines the ν_1 width of the 2D spectrum rather than its maximum ν_1 value. Therefore, the measurement times are greatly reduced by choosing appropriate coherence time steps.

In order to compute a 2D spectrum, the signal amplitude and phase of one data set containing a full τ -scan at a defined population time T are extracted by a Fourier analysis that is described in detail elsewhere [61–63]. Briefly, the signal is first Fourier-transformed along ω_{Det} into the time domain. Only the positive time components are chosen by a supergaussian filter function for causality reasons. After transforming the signal back to the spectral domain, the local oscillator field amplitude is divided out. 2D spectra are obtained by a Fourier transform along the coherence time axis. For proper extraction of the signals, the relative phase between the signal and the local oscillator have to be known exactly. In a phasing procedure, the 2D spectrum integrated along the excitation-frequency axis is compared to a pump-probe spectrum measured at the same population time. The spectral interferogram is then multiplied with a constant phase and two linear phase terms that take into account the uncertainty of relative timing between k_1 and k_2 as well as k_3 and k_{LO} . Changing the phase parameters leads to proper phasing that is assumed to be achieved when the integrated 2D spectrum fits the pump-probe spectrum [30].

2.3.3 Two-Color Pump-Probe Setup

Figure 2.13 depicts the setup to perform two-color pump-probe measurements. Two independently tunable OPAs (Sect. 2.3.1) serve as sources for pump and probe pulses. The pump-probe delay time corresponding to the population time T is introduced by a mechanical delay stage in the pump arm. Probe pulses from the OPA are attenuated and split into a probe and a reference by taking the front- and back-surface-reflection of a BaF₂ wedge. Pump and probe pulses with pulse energies of about 2 μ J and a few tens of nJ, respectively, are focussed into the same spot in the sample by 30° off-axis parabolic mirrors (spot size $\approx 100 \mu\text{m}$). The probing of homogeneously excited sample volumes is realized by tighter focussing of the probe beam. In practice, increasing the probe beam waist with a telescope before focussing leads to smaller spot sizes in the sample. The reference pulse is transmitted through the sample at a different position. After the sample interaction the probe beam is dispersed by a monochromator and detected with a 64-pixel MCT array. Chopping the pump beam at 500 Hz and using the reference pulse for correction of probe-pulse intensity fluctuations, we calculate the transient absorbance change ΔA as a function of the delay time T and the probe frequency ν_{Pr} (equivalent to the detection frequency of 2D spectra):

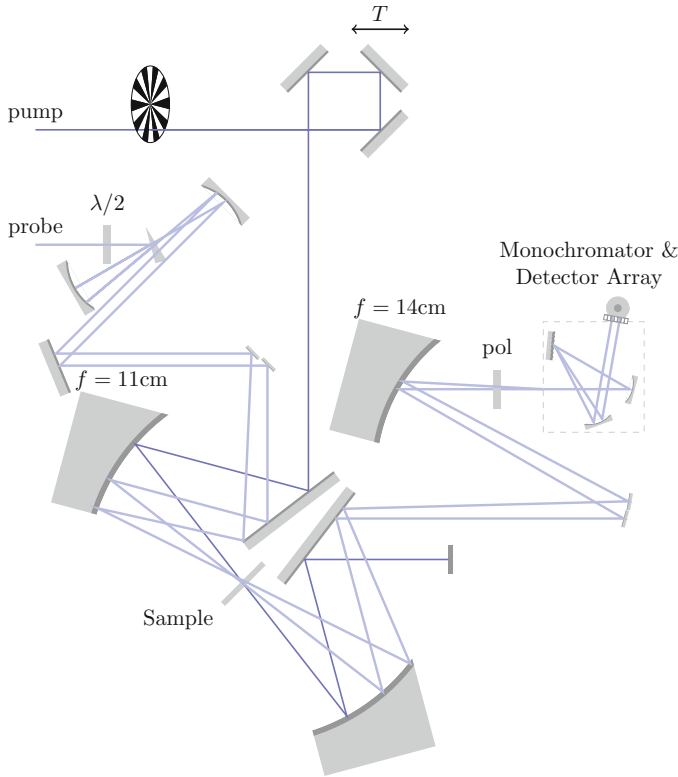


Fig. 2.13 Sketch of the two-color pump-probe setup. Pump and probe pulses are generated in two independently tuneable OPAs. A translation stage in the pump beam path allows for control of the pump-probe delay T . Probe and reference pulses are obtained by taking the reflection of two sides of a BaF₂ wedge. Spectrally-resolved pump-induced absorbance changes are measured by overlapping probe pulses with chopped pump pulses (500 Hz) in the same spot of the sample and detecting the probe with a monochromator and 64-pixel MCT array. A second array measures the reference pulse intensities (without pump overlap) simultaneously in order to correct for intensity fluctuations. For polarization-resolved measurements, the probe is polarized under a 45° angle with respect to the pump by a half-wave plate ($\lambda/2$). A polarizer (pol) then allows for detecting absorbance changes with arbitrary relative polarization compared to the pump pulses

$$\Delta A(T, \nu_{Pr}) = -\log \left(\frac{I_{pump}^{(probe)}(T, \nu_{Pr})}{I_0^{(probe)}(T, \nu_{Pr})} \cdot \frac{I_0^{(reference)}(T, \nu_{Pr})}{I_{pump}^{(reference)}(T, \nu_{Pr})} \right) \quad (2.70)$$

Here the subscripts *pump* and 0 indicate intensities with and without pump excitation, and the superscripts denote intensities from the probe and the reference, respectively. Equation 2.70 is evaluated on a shot-to-shot basis to avoid contributions from pulse energy fluctuations.

In single-color measurements, significant interference fringes due to scattering of the pump beam can occur. Those signals cannot be eliminated in the same way as in the 2D IR setup. Instead, moving the pump-probe delay in fractions of the wavelength and averaging over an oscillation period helps to suppress interferences. Since the wavelength of the pulses used in this thesis is $<10\mu\text{m}$, the reduction in time resolution ($<33\text{ fs}$) is negligible.

Polarization-resolved measurements are performed by inserting a half-wave plate into the probe beam path and thereby polarizing the probe under a 45° angle with respect to the pump. Polarization analysis of the emitted signal is the basis for a construction of the pump-probe anisotropy (cf. Eq. 2.62):

$$r(T) = \frac{\Delta A_{||}(T) - \Delta A_{\perp}(T)}{\Delta A_{||}(T) + 2 \cdot \Delta A_{\perp}(T)} \quad (2.71)$$

Absorbance changes parallel $\Delta A_{||}(T)$ and perpendicular $\Delta A_{\perp}(T)$ to the pump polarization are selected with a polarizer after the sample interaction.

The experimental setup is placed in a sealed box that can be purged with nitrogen to prevent infrared absorption by water vapor or carbon dioxide in air (cf. Fig. 2.2a, green line).

2.3.4 Phospholipid Reverse Micelles

The central focus of this thesis are phospholipid reverse micelles made of 1,2-dioleoyl-sn-glycero-3-phosphocholine (DOPC) as depicted in Fig. 2.14 for the study of phosphate-water interactions and structural fluctuations of confined water on ultra-fast time scales. However, such aggregates can also be formed by other surfactants. In fact, the molecule investigated most extensively is dioctyl sodium sulfosuccinate (aerosol OT, AOT, cf. Fig. 2.14) [64] that was initially synthesized as a wetting agent to reduce the surface tension of water e.g., for the use as washing powder or modification of the floating properties of swimming objects [65, 66]. Reverse micelles are ideal tools to embed nanoscopic water pools in nonpolar solvents with the water content determining their size [67, 68]. Therefore, an important parameter to characterize such systems is the relative water concentration

$$w_0 = \frac{[\text{water}]}{[\text{surfactant}]} \quad (2.72)$$

where the brackets indicate molar concentrations. It has been shown for AOT [69, 70] that the reverse-micelle diameter d_{RM} scales linearly with w_0 up to a value of $w_0 = 30$:

$$d_{RM} = cw_0 + d_0 \quad (2.73)$$

molecules interact with the charged interface and are highly immobilized compared to bulk water whose behavior is approached by increasing the value of w_0 [71–73]. AOT is the workhorse of reverse-micelle studies [74, 75] but it has also been shown that different phospholipids self-assemble into reverse-micelle structures [76].

For the preparation of phospholipid reverse micelles used in the time-resolved experiments presented in Chaps. 3 and 4, DOPC was dissolved in benzene with a concentration of 0.25 M. Appropriate amounts of water were added in order to obtain samples in a wide range of hydration between $w_0 = 1$ and 16. Dynamic light scattering of solutions at $w_0 = 5$ and 16.5 indicate reverse-micelle diameters of (4.65 ± 0.15) and (7.9 ± 0.5) nm, respectively. Assuming a linear relationship as in Eq. 2.73 we extract $c = (0.30 \pm 0.02)$ nm and $d_0 = (3.2 \pm 0.2)$ nm, i.e., the growth of DOPC reverse micelles with w_0 is similar to the well-known AOT case. The value of d_0 agrees reasonably with the 3.6 nm thickness of fully hydrated DOPC bilayers [77]. Values for reverse micelle diameters in the hydration range of $w_0 = 1 - 16$ used for the time-resolved experiments in this work vary between 3.5 and 8 nm (cf. Table 2.1). The number of DOPC molecules per reverse micelle varies between 60–300. This parameter is determined by the ratio of the reverse-micelle surface area and the area of a DOPC molecule which is assumed to increase linearly with w_0 between 0.6 and 0.7 nm^2 according to the results obtained by phospholipid hydration. The water pool size increases from ≈ 60 ($w_0 = 1$) to 4600 ($w_0 = 16$) H_2O molecules. Increasing reverse micelle volumes (V_{RM}) lead to decreasing reverse micelle concentrations and therefore a larger space that a single reverse micelle can take up (V_{space}). Table 2.1 lists these parameters as a function of w_0 suggesting that the sample may be thought of as mainly non-interacting particles at the DOPC concentration used in the experiments.

While the hydration structure of phospholipids in aqueous solution is well characterized, less is known about water structure in reverse-micellar systems. However, it is conceivable that the main characteristics of the lipid head-group organization and hydration structure in these systems, i.e., the hydration sites, hydrogen-bond strengths and the occurrence of inter- and intramolecular charge pairs, are comparable. The typical behavior of water in confinement was found for phospholipid reverse

Table 2.1 Parameters of the DOPC reverse-micelle system at a concentration of 0.25 M in benzene as a function of hydration (w_0): diameter (d_{RM} , Eq. 2.73), number (#) of DOPC and water molecules per reverse micelle, volume of a reverse micelle (V_{RM}) and the average free volume determined from the reverse-micelle concentration (V_{space})

w_0	d_{RM} (nm)	# DOPC	# H_2O	V_{RM} (nm^3)	V_{space} (nm^3)
1	3.5	64	64	22	428
3	4.1	86	258	36	574
5	4.7	111	554	54	738
8	5.6	152	1219	92	1016
16	8.0	287	4596	268	1915

micelles [78, 79], i.e., immobilized water interacting with the lipid head groups at low hydration levels and a buildup of bulk-like water pools after full hydration of the phospholipid head groups ($w_0 > 6-8$).

Most of this thesis deals with ultrafast dynamics inside DOPC reverse micelles. However, it is sometimes instructive to compare the results to systems containing different surfactant molecules (cf. Fig. 2.14, bottom). The permanent charges of ionic surfactants cause electrostatic potentials in which water molecules align as described in Sect. 1.1. As a result, interface-bound water experiences a markedly different environment compared to the bulk that affects intermolecular vibrations such as librations, i.e., hindered rotations.

An important difference between DOPC and AOT is the configuration of the head group. DOPC has a zwitterionic structure where the N^+ counterion is an integrated part of the phospholipid molecule whereas the Na^+ counterions of AOT are free. Therefore, the DOPC head-group volume is significantly larger than the one of AOT. Indeed, solvation dynamics suggest that water reorientation in lecithin reverse micelles is more restricted than for AOT at similar hydration levels due to the higher amount of water accepted by the lecithin interface [80]. Moreover, hydrogen bonds of water interacting with AOT head groups were found to be weaker than bulk-water hydrogen bonds [81] in contrast to the stronger hydrogen bonds at phospholipid interfaces.

The effect of charged head groups may be independently tested by non-ionic surfactants with head groups consisting of polyoxyethylenes and a glycol group such as glycol dodecyl ether (Brij-30, Fig. 2.14). While non-ionic reverse micelles are significantly less studied than their ionic counterparts, it is known that water forms pools inside Brij-30 reverse micelles [82, 83]. A non-uniform water distribution in the Brij-30 micelle core was found with only little penetration into the polyoxyethylene-chain region and increased water mobility compared to anionic reverse micelles.

References

1. M. Born, R. Oppenheimer, Zur Quantentheorie der Molekeln. German. Ann. Phys. **389**, 457–484 (1927)
2. G. Herzberg, *Molecular Spectra and Molecular Structure I Spectra of Diatomic Molecules* (D. Van Nostrand Company Inc, New York, 1950)
3. G. Herzberg, *Molecular Spectra and Molecular Structure II Infrared and Raman Spectra of Polyatomic Molecules* (Krieger Publishing Company, Malabar, 1991)
4. P. Hamm, M. Zanni, *Concepts and Methods of 2D Infrared Spectroscopy* (Cambridge University Press, Cambridge, 2011)
5. L. Pauling, E.B. Wilson, *Introduction to Quantum Mechanics* (McGraw-Hill Book Company, Inc., New York, 1935)
6. E. Schrödinger, Quantisierung als Eigenwertproblem. German. Ann. Phys. **384**, 489–527 (1926)
7. E. Fermi, Über den Ramaneffekt des Kohlendioxyds. German. Z. Phys. **71**, 250–259 (1931)
8. C.V. Raman, The molecular scattering of light. Nobel Lecture (1930)
9. B.S. Hudson, Vibrational spectroscopy using inelastic neutron scattering: overview and outlook. Vib. Spectrosc. **42**, 25–32 (2006)

10. R.G. Gordon, Correlation functions for molecular motion. *Adv. Magn. Reson.* **3**, 1–42 (1968)
11. P.W. Anderson, P.R. Weiss, Exchange narrowing in paramagnetic resonance. *Rev. Mod. Phys.* **25**, 269–276 (1953)
12. R. Kubo, A stochastic theory of line-shape and relaxation, in *Fluctuation, Relaxation and Resonance in Magnetic Systems*, ed. by D. ter Haar (Oliver & Boyd, Edinburgh, 1962)
13. R. Kubo, A stochastic theory of lineshape. *Adv. Chem. Phys.* **15**, 101–127 (1969)
14. W.G. Rothschild, Motional characteristics of large molecules from their Raman and infrared band contours: vibrational dephasing. *J. Chem. Phys.* **65**, 455–462 (1976)
15. N. Bloembergen, E.M. Purcell, R.V. Pound, Relaxation effects in nuclear magnetic resonance absorption. *Phys. Rev.* **73**, 679–712 (1948)
16. P.A.M. Dirac, The quantum theory of the emission and absorption of radiation. *Proc. R. Soc. Lond., Ser. A* **114**, 243–265 (1927)
17. D.W. Oxtoby, Vibrational population relaxation in liquids. *Adv. Chem. Phys.* **47**, 487–519 (1981)
18. B.J. Berne, Time-dependent properties of condensed media, in *Physical Chemistry: An Advanced Treatise*, vol. 8B, ed. by D. Henderson (Academic, New York, 1971), pp. 540–713
19. J.S. Bader, B.J. Berne, Quantum and classical relaxation rates from classical simulations. *J. Chem. Phys.* **100**, 8359–8366 (1994)
20. J.L. Skinner, Semiclassical approximations to golden rule rate constants. *J. Chem. Phys.* **107**, 8717–8718 (1997)
21. W.S. Benedict, E.K. Plyler, Absorption spectra of water vapor and carbon dioxide in the region of 2.7 microns. *J. Res. Natl. Bur. Stand.* **46**, 246–259 (1951)
22. A. Novak, Hydrogen bonding in solids correlation of spectroscopic and crystallographic data, *Large Molecules*, vol. 18, Structure and Bonding (Springer, Berlin, 1974), pp. 177–216
23. C.M. Huggins, G.C. Pimentel, Systematics of the infrared spectral properties of hydrogen bonding systems: frequency shift, half width and intensity. *J. Phys. Chem.* **60**, 1615–1619 (1956)
24. S. Mukamel, *Principles of Nonlinear Optical Spectroscopy* (Oxford University Press, Oxford, 1995)
25. M. Cho, *Two-dimensional Optical Spectroscopy* (CRC Press, Taylor & Francis Group, Boca Raton, 2009)
26. R.W. Boyd, *Nonlinear Optics*, 3rd edn. (Elsevier, 2008)
27. M.D. Fayer, Dynamics of molecules in condensed phases: Picosecond holographic grating experiments. *Annu. Rev. Phys. Chem.* **33**, 63–87 (1982)
28. K. Duppen, D.A. Wiersma, Picosecond multiple-pulse experiments involving spatial and frequency gratings: a unifying nonperturbational approach. *J. Opt. Soc. Am. B* **3**, 614–621 (1986)
29. S.A. Corcelli, J.L. Skinner, Infrared and Raman line shapes of dilute HOD in liquid H₂O and D₂O from 10 to 90°C. *J. Phys. Chem. A* **109**, 6154–6165 (2005)
30. S.M. Gallagher Faeder, D.M. Jonas, Two-dimensional electronic correlation and relaxation spectra: Theory and model calculations. *J. Phys. Chem. A* **103**, 10489–10505 (1999)
31. M. Khalil, N. Demirdöven, A. Tokmakoff, Obtaining absorptive line shapes in two-dimensional infrared vibrational correlation spectra. *Phys. Rev. Lett.* **90**, 047401 (2003)
32. K. Okumura, A. Tokmakoff, Y. Tanimura, Two-dimensional line-shape analysis of photon-echo signal. *Chem. Phys. Lett.* **314**, 488–495 (1999)
33. A. Tokmakoff, Two-dimensional line shapes derived from coherent third-order nonlinear spectroscopy. *J. Phys. Chem. A* **104**, 4247–4255 (2000)
34. K. Kwak, S. Park, I.J. Finkelstein, M.D. Fayer, Frequency-frequency correlation functions and apodization in two-dimensional infrared vibrational echo spectroscopy: a new approach. *J. Chem. Phys.* **127**, 124503 (2007)
35. K. Lazonder, M.S. Pshenichnikov, D.A. Wiersma, Easy interpretation of optical two-dimensional correlation spectra. *Opt. Lett.* **31**, 3354–3356 (2006)
36. K. Kwak, M. Cho, Two-color pump-probe spectroscopies of two- and three-level systems: 2-dimensional line shapes and solvation dynamics. *J. Phys. Chem. A* **107**, 5903–5912 (2003)

37. G. Stirnemann, J.T. Hynes, D. Laage, Water hydrogen bond dynamics in aqueous solutions of amphiphiles. *J. Phys. Chem. B* **114**, 3052–3059 (2010)
38. A. Ghosh, R.M. Hochstrasser, A peptide's perspective of water dynamics. *Chem. Phys.* **390**, 1–13 (2011)
39. M. Khalil, A. Tokmakoff, Signatures of vibrational interactions in coherent two-dimensional infrared spectroscopy. *Chem. Phys.* **266**, 213–230 (2001)
40. S. Woutersen, P. Hamm, Nonlinear two-dimensional vibrational spectroscopy of peptides. *J. Phys.: Condens. Matter* **14**, R1035–R1062 (2002)
41. M. Chachisvilis, H. Fidder, V. Sundström, Electronic coherence in pseudo twocolour pump-probe spectroscopy. *Chem. Phys. Lett.* **234**, 141–150 (1995)
42. T. Tao, Time-dependent fluorescence depolarization and Brownian rotational diffusion coefficients of macromolecules. *Biopolymers* **8**, 609–632 (1969)
43. G.R. Fleming, J.M. Morris, G.W. Robinson, Direct observation of rotational diffusion by picosecond spectroscopy. *Chem. Phys.* **17**, 91–100 (1976)
44. H. Graener, G. Seifert, A. Laubereau, Direct observation of rotational relaxation times by time-resolved infrared spectroscopy. *Chem. Phys. Lett.* **172**, 435–439 (1990)
45. P.F. Moulton, Spectroscopic and laser characteristics of Ti:Al₂O₃. *J. Opt. Soc. Am. B* **3**, 125–133 (1986)
46. R.A. Kaindle, M. Wurm, K. Reimann, P. Hamm, A.M. Weiner, M. Woerner, Generation, shaping, and characterization of intense femtosecond pulses tunable from 3 to 20 μm . *J. Opt. Soc. Am. B* **17**, 2086–2094 (2000)
47. R. Trebino, *Frequency-resolved Optical Gating: The Measurement of Ultrashort Laser Pulses* (Kluwer Academic, Boston, 2000)
48. R. Trebino, K.W. DeLong, D.N. Fittinghoff, J.N. Sweetser, M.A. Krumbügel, B.A. Richman, D.J. Kane, Measuring ultrashort laser pulses in the timefrequency domain using frequency-resolved optical gating. *Rev. Sci. Instrum.* **68**, 3277–3295 (1997)
49. C. Iaconis, I.A. Walmsley, Spectral phase interferometry for direct electric-field reconstruction of ultrashort optical pulses. *Opt. Lett.* **23**, 792–794 (1998)
50. G. Stibenz, P. Staudt, C. Lukas, S.-P. Gorza, and I. A. Walmsley, Fully automated, phase corrected long crystal SPIDER for the characterization of broadband pulses, in *Conference on Lasers and Electro-Optics/Quantum Electronics and Laser Science Conference and Photonic Applications Systems Technologies* (2008)
51. Q. Wu, X.-C. Zhang, Free-space electro-optic sampling of terahertz beams. *Appl. Phys. Lett.* **67**, 3523–3525 (1995)
52. P. Hamm, M. Lim, R.M. Hochstrasser, Structure of the amide I band of peptides measured by femtosecond nonlinear-infrared spectroscopy. *J. Phys. Chem. B* **102**, 6123–6138 (1998)
53. M.L. Cowan, J.P. Ogilvie, R.J.D. Miller, Two-dimensional spectroscopy using diffractive optics based phased-locked photon echoes. *Chem. Phys. Lett.* **386**, 184–189 (2004)
54. T. Brixner, T. Mančal, I.V. Stiopkin, G.R. Fleming, Phase-stabilized twodimensional electronic spectroscopy. *J. Chem. Phys.* **121**, 4221–4236 (2004)
55. V. Volkov, R. Schanz, P. Hamm, Active phase stabilization in Fourier-transform two-dimensional infrared spectroscopy. *Opt. Lett.* **30**, 2010–2012 (2005)
56. L.P. DeFlores, R.A. Nicodemus, A. Tokmakoff, Two-dimensional Fourier transform spectroscopy in the pump-probe geometry. *Opt. Lett.* **32**, 2966–2968 (2007)
57. J. Helbing, P. Hamm, Compact implementation of Fourier transform twodimensional IR spectroscopy without phase ambiguity. *J. Opt. Soc. Am. B* **28**, 171–178 (2011)
58. S.-H. Shim, M.T. Zanni, How to turn your pump-probe instrument into a multidimensional spectrometer: 2D IR and Vis spectroscopies via pulse shaping. *Phys. Chem. Chem. Phys.* **11**, 748–761 (2009)
59. W. Kuehn, K. Reimann, M. Woerner, T. Elsaesser, R. Hey, Two-dimensional terahertz correlation spectra of electronic excitations in semiconductor quantum wells. *J. Phys. Chem. B* **115**, 5448–5455 (2011)
60. C.E. Shannon, Communication in the presence of noise. *Proc. IEEE* **37**, 10–21 (1949)

61. L. Lepetit, G. Chériaux, M. Joffre, Linear techniques of phase measurement by femtosecond spectral interferometry for applications in spectroscopy. *J. Opt. Soc. Am. B* **12**, 2467–2474 (1995)
62. N. Huse, Multidimensional vibrational spectroscopy of hydrogen-bonded systems in the liquid phase: Coupling mechanisms and structural dynamics. Ph.D. thesis. Humboldt Universität zu Berlin, 2006
63. M. Yang, Ultrafast two-dimensional infrared spectroscopy of hydrogen-bonded base pairs and hydrated DNA. Ph.D. thesis. Humboldt Universität zu Berlin, 2012
64. T.K. De, A. Maitra, Solution behaviour of Aerosol OT in non-polar solvents. *Adv. Colloid Interface Sci.* **59**, 95–193 (1995)
65. C.R. Caryl, Sulfosuccinic esters. Structure and wetting power. *Ind. Eng. Chem.* **33**, 731–737 (1941)
66. C.R. Caryl, W.P. Ericks, Esters of sodium sulfosuccinic acid. *Ind. Eng. Chem.* **31**, 44–47 (1939)
67. R.W. Mattoon, M.B. Mathews, Micelles in non-aqueous media. *J. Chem. Phys.* **17**, 496–497 (1949)
68. M.B. Mathews, E. Hirschhorn, Solubilization and micelle formation in a hydrocarbon medium. *J. Colloid Sci.* **8**, 86–96 (1953)
69. M. Zulauf, H.F. Eicke, Inverted micelles and microemulsions in the ternary system water/Aerosol-OT/isooctane as studied by photon correlation spectroscopy. *J. Phys. Chem.* **83**, 480–486 (1979)
70. M.-P. Pileni, T. Zemb, C. Petit, Solubilization by reverse micelles: solute localization and structure perturbation. *Chem. Phys. Lett.* **118**, 414–420 (1985)
71. M. Wong, J.K. Thomas, T. Nowak, Structure and state of water in reversed micelles. 3. *J. Am. Chem. Soc.* **99**, 4730–4736 (1977)
72. R.E. Riter, D.M. Willard, N.E. Levinger, Water immobilization at surfactant interfaces in reverse micelles. *J. Phys. Chem. B* **102**, 2705–2714 (1998)
73. J. Faeder, B.M. Ladanyi, Molecular dynamics simulations of the interior of aqueous reverse micelles. *J. Phys. Chem. B* **104**, 1033–1046 (2000)
74. P.L. Luisi, M. Giomini, M.P. Pileni, B.H. Robinson, Reverse micelles as hosts for proteins and small molecules. *Biochim. Biophys. Acta, Rev. Biomembr.* **947**, 209–246 (1988)
75. M.P. Pileni, Reverse micelles as microreactors. *J. Phys. Chem.* **97**, 6961–6973 (1993)
76. P. Walde, A.M. Giuliani, C.A. Boicelli, P.L. Luisi, Phospholipid-based reverse micelles. *Chem. Phys. Lipids* **53**, 265–288 (1990)
77. N. Kučerka, S. Tristram-Nagle, J.F. Nagle, Structure of fully hydrated fluid phase lipid bilayers with monounsaturated chains. *J. Membr. Biol.* **208**, 193–202 (2006)
78. C.A. Boicelli, M. Giomini, A.M. Giuliani, Infrared characterization of different water types inside reverse micelles. *Appl. Spectrosc.* **38**, 537–539 (1984)
79. V.V. Kumar, P. Raghunathan, Proton NMR studies of the interaction of water with lecithin in non-polar organic media. *Chem. Phys. Lipids* **41**, 159–171 (1986)
80. D.M. Willard, R.E. Riter, N.E. Levinger, Dynamics of polar solvation in lecithin/water/cyclohexane reverse micelles. *J. Am. Chem. Soc.* **120**, 4151–4160 (1998)
81. G. Onori, A. Santucci, IR investigations of water structure in Aerosol OT reverse micellar aggregates. *J. Phys. Chem.* **97**, 5430–5434 (1993)
82. H. Caldararu, A. Caragheorgheopol, M. Vasilescu, I. Dragutan, H. Lemmetyinen, Structure of the polar core in reverse micelles of nonionic poly(oxyethylene) surfactants, as studied by spin probe and fluorescence probe techniques. *J. Phys. Chem.* **98**, 5320–5331 (1994)
83. D. Pant, N.E. Levinger, Polar solvation dynamics in nonionic reverse micelles and model polymer solutions. *Langmuir* **16**, 10123–10130 (2000)

Ultrafast Dynamics of Phospholipid-Water Interfaces
Studied by Nonlinear Time-Resolved Vibrational
Spectroscopy

Costard, R.

2015, X, 103 p. 42 illus., 6 illus. in color., Hardcover

ISBN: 978-3-319-22065-9